HEAT TREATMENT OF LONG PRODUCTS

Horský J.[1]*, Raudenský M.[1], Chabičovský M.[1] and Šimeček P.[2]
*Author for correspondence
[1]Heat Transfer and Fluid Flow Laboratory,
Faculty of Mechanical Engineering, Brno University of Technology,
Technická 2, 61669 Brno,
Czech Republic,
[2]ITA Ltd.,
Martinská 6, 709 00 Ostrava,
Czech Republic,
E-mail: horsky@fme.vutbr.cz

ABSTRACT

An in-line heat treatment of rolled materials is becoming frequently used by hot rolling plants. This method achieves the required material structure without the necessity of reheating.

This paper describes a design procedure of cooling sections for obtaining the demanded structure and mechanical properties.

Experimental stands, applied for the cooling study of steel samples, were built at the Brno University of Technology. The first experimental stand enables to simulate a variety of cooling regimes and evaluate the final structure of the tested samples which are instrumented by set of thermocouples indicating the temperature history of the tested material. The second experimental stand is a tool for the design of the cooling sections which can ensure obtaining demanded heat treatment procedure and demanded final structure. The heat transfer coefficient history at the surface is gained as an output of the inverse task.

Mathematical model and its implementation into the software tool for computer simulation of heat treatment processes (quenching and tempering) of steel is presented. Heat transfer boundary conditions obtained from test on experimental stand are used for calculation of cooling curves followed by prediction of microstructure after austenite transformation and final mechanical properties as hardness, tensile strength and yield stress. The software QTSteel used for computer simulation of heat treatment of long products has been developed by ITA Ltd. Verification and practical examples of metallurgical predictions for long products, especially tubes and bars, are presented.

INTRODUCTION

Microstructure and nature of grains, grain size and composition determine the overall mechanical behaviour of the steel. Heat treatment provides an efficient way to manipulate the properties of steel by controlling the cooling rate. The way of heat treatment depends on many aspects. One of the most important parameter is the amount of production. Another important parameter is the size of products. We focus here on large production such as cooling of long products at the exit from a rolling mill, cooling of rails, tubes and special profiles. Such a treatment is called in-line heat treatment of materials and has become frequently used by hot rolling plants. This method achieves the required material structure without the necessity of reheating. In-line heat treatment is characterized by running of hot material through the cooling section. However, many of discussed topics can be applied on smaller production as well.

The design procedure of cooling sections for obtaining the demanded structure and mechanical properties is iterative research involving several important steps. We begin with the Continuous Cooling Transformation (CCT) diagram for the selected material. Numerical simulation of the cooling follows to find appropriate cooling intensity and its duration. Knowing the desired cooling intensity new cooling section is designed and tested under the laboratory conditions. From the laboratory experiments boundary conditions are obtained and tested using a numerical model [1]. When the best solution is found it is tested on the real sample and the result structure is studied. In most cases the process must be repeated as the CCT diagram is aimed at a different size of the sample and the cooling rate in the designed section is not constant.

PREDICTION OF HARDNESS AND MICROSTRUCTURE

The MetaCool is the library of functions that enables prediction of mechanical properties and microstructure of heat treated steel. The data interface contains pure physical quantities on the input (chemistry, temperatures, times, strains, cooling curve) and microstructure fractions and final mechanical properties of the steel (hardness, yield stress, ultimate tensile strength) as output [2]. MetaCool is divided internally into 17 steel groups and covers carbon and structural steels with amount of carbon from 0.08% to 0.6% and with the total sum of alloying additions up to 10%. Assigning of the steel with specified chemical composition into particular group is performed automatically and metallurgical algorithms differ from one steel group to another.

The CCT diagram model

The model of the CCT (continuous cooling transformation) diagram consists of the set of lines (significant temperatures: Ac_3 - Temperature at which ferrite completes its transformation

into austenite, Ac_1 - Temperature at which austenite begins to form, *Ms* - Martensite start temperature) and curves (unsymmetrical parabolas) specified by time and temperature coordinates of their significant points (nose, upper and lower branch). The position of lines and curves in the CCT diagram for specified chemistry was acquired from published diagrams processed separately for each steel group with the use of regression analysis.

Temperature curve and transformation kinetics

Transformation kinetics of diffusion processes is described by the Avrami equation (1) which was modified for cases of cooling curves with non-uniform cooling rates

$$X(t,T) = X_\gamma\left(1 - \exp\left(-k(T)t^{n(T)}\right)\right) \quad (1)$$

where parameters *k(T)* and *n(T)* depend on the cooling rate, t is the time and X_γ is the rest of austenite. With the use of (1) the percentage of ferrite, pearlite and bainite is calculated in accordance with intersections of the cooling curve with particular CCT curves. It is supposed that the cooling curve does not need to be uniformly decreasing.

Process of martensitic transformation is not time dependent so the standard Koistinen-Marburger equation (2) is used

$$X_M(T) = (1 - \exp(-b(TMs - T)^n))X_\gamma \quad (2)$$

where b and n are constants, *TMs* is the Martensite start temperature and X_γ is the rest of austenite.

Mechanical properties prediction

Basic step for prediction of final mechanical properties is the calculation of the HV hardness. The HV hardness after hardening has been determined by regression analysis for the shape function (3) with the percentage of alloying addition c_i, amount of particular structure fraction X_{struc} (X_F – structure fraction of the ferrite, X_P – structure fraction of the pearlite, X_B – structure fraction of the bainite and X_M – structure fraction of the martensite) and constants C_0, D_i, E_i, F_i and G_i :

$$HV = C_0 + X_F + \sum_i D_i c_i + X_P \sum_i E_i c_i + X_B \sum_i F_i c_i + X_M \sum_i G_i c_i \quad (3)$$

Relationship between HV and ultimate tensile strength is well known. The calculation of yield stress is more difficult. It also reflects the ferrite grain size effect in v Hall-Petch equation and influence of the cooling rate CR on the transformation of austenite and amount of structure fraction X_{struci}:

$$R_e = f\left(d_\alpha, CR, X_F, \sum(X_P + X_B + X_M)\right) \quad (4)$$

Tempered mechanical properties are calculated from the chemistry $c_{(i)}$ by the equation (5) based on the regression analysis of HV hardness of particular structure fraction for various tempering temperatures T_{temp} but fixed tempering time 3hrs

$$HVx_3 = \left\{\sum_i R_{(i)}\right\}_{Ttemp,3hrs} \quad (5)$$

The standard Hollomon-Jaffe parameter H_p is used for calculation of equivalent tempering regime with various tempering times and temperatures

$$H_P = \left(T_{temp} + 273.15\right) \times \frac{(C + \log\, t_{temp})}{1000} \quad (6)$$

where C is a constant varying between 15 and 21.

EXPERIMENTAL DETERMINATION OF SPRAY COOLING INTENSITY

The cooling intensity of spray is a function of several parameters, like nozzle type, flow rate, water pressure, surface temperature of a material, and velocity of a material movement whilst under spray. There is no function available which describes cooling intensity using all the mentioned parameters and so real measurement is only one way for determination of spray cooling intensity. The determination of the spray cooling intensity consists of several steps: preparation of the experiment, experimental measurement, calculation of boundary condition and evaluation of computed results.

Experiment

The experimental procedure starts with manufacturing of the test sample and embedding of thermocouples to the test sample. The test sample is mounted to the experimental apparatus and then it is heated to required temperature. When the test sample is heated the spray is started. When the cooling conditions are adjusted the data-logger starts to record temperatures of thermocouples and the sample mounted on trolley is passing through the cooling section repeatedly. When the sample is cooled down, recorded data are transferred to computer and processed to evaluation.

Calculating of boundary condition

After measurement the inverse heat conduction problem is used to compute time dependent boundary conditions: heat transfer coefficient and surface temperature. Beck's sequential approach is used for it [3] and [4]. This method uses sequential estimation of the time varying boundary conditions and future time steps. First the sum of squares error is computed using f future time steps when the measured temperatures T_i^* are compared with the computed temperatures T_i at the current time m:

$$SSE = \sum_{i=m+1}^{m+f} (T_i^* - T_i)^2 \quad (7)$$

Temperatures T_i are computed from forward solver e.g. FDM, FEM, FVM. Then surface heat flux q in time m is calculate by minimizing equation (7) using the linear minimization theory

$$q^m = \frac{\sum_{i=m+1}^{m+f}\left(T_i^* - T_i|_{q^m=0}\right)\zeta_i}{\sum_{i=m+1}^{m+f}(\zeta_i)^2} \quad (8)$$

where $T_i|_{q^m=0}$ are the temperatures in the thermocouple, which have been embedded in the sensor, and computed from the forward solver using all previously computed heat fluxes without q^m. ζ_i is the sensitivity of the sensor with thermocouple at time index i to the heat flux pulse at time m. These sensitivity coefficients physically indicate increase of temperature in the thermocouple per unit of heat flux at the surface. Sensitivity coefficient is defined as

$$\zeta_i = \frac{\partial T_i}{\partial q^m} \quad (9)$$

The heat transfer coefficient (HTC) can be computed when surface temperatures T_0^m and surface heat fluxes q^m are known:

$$HTC^m = \frac{q^m}{T_\infty^m - (T_0^m - T_0^{m-1})/2} \quad (10)$$

T_∞^m is ambient temperature.

Results

The measured time dependent temperature is used as input for inverse heat conduction problem and time dependent surface temperature, heat flux and heat transfer coefficient are obtained (Figure 1). Further the dependence of the heat transfer coefficient on the surface temperature and position in the cooling section is obtained. The average value of the heat transfer coefficient along the position is shown in Figure 2.

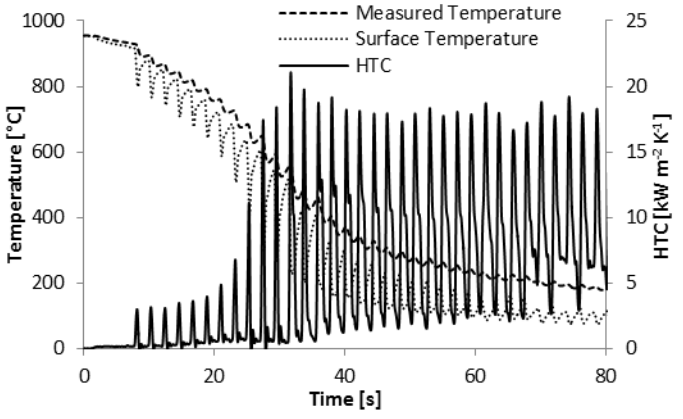

Figure 1 Example of measured temperature, computed surface temperature and heat transfer coefficient depending on the time

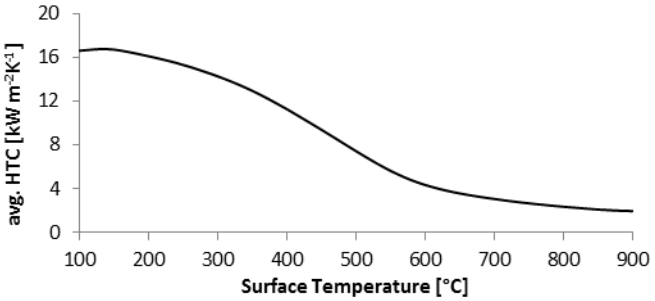

Figure 2 The dependence of the average heat transfer coefficient on the surface temperature

FINDING THE OPTIMAL COOLING REGIME

It is necessary to achieve required cooling regime for obtaining required mechanical properties of final product. The numerical prediction of hardness and microstructure can serve as initial information about the required cooling regime. It is necessary to validate the predicted hardness and microstructure by the real test. Tests in industry conditions are very expensive and so it is more suitable to conduct some tests with smaller samples in laboratory. The scale factor is important and the sample should have the same thickness and shape of the final product. The type of nozzle and feeding pressure are the parameters used to define the resulting cooling intensity, which will cause required material structure. The experimental apparatus is able to cool the sample in a wide range of regimes. The cooling regime can be modified until optimal structure of the material is achieved.

Numerical prediction of hardness and microstructure

The software QTSteel [5] can be used for numerical prediction of metallurgical processes running during examined and optimized cooling regimes. It is the off-line tool for calculation of microstructure and mechanical properties of various bodies after hardening and subsequent tempering. Metallurgical functionality of QTSteel is based on the MetaCool library described in the beginning of this article.

Experimental apparatus and experimental process

A test bench was built for the purpose of finding the optimal cooling strategy for given steel (Figure 3). It was composed of an electric furnace, a nozzle, a rail with a moveable test steel sample and a deflector.

The steel sample with dimensions 50 x 50 x 62 mm was made of 20MnV6 steel. It was embedded by four thermocouples positioned 3, 12, 21 and 50 mm under the cooled surface. The steel sample was heated to an initial temperature in an electric furnace with an inert atmosphere to avoid oxidation. The heated sample was then moved into a cooling position under the nozzle and pneumatically driven deflector was opened and cooling of the hot sample started (Figure 4). Temperatures at a given positions were measured by thermocouples and recorded by data-logger during the experiment. Recorded temperatures are shown in Figure 5.

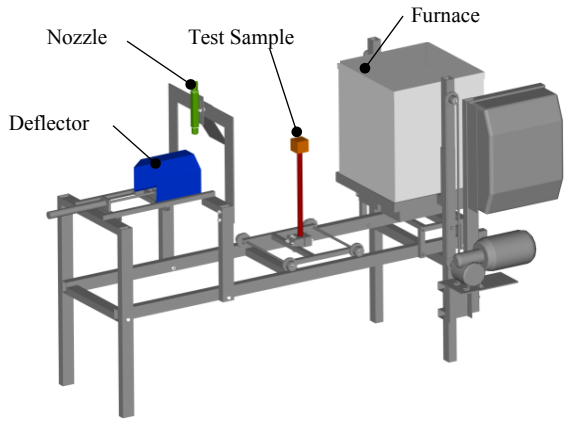

Figure 3 Experimental apparatus

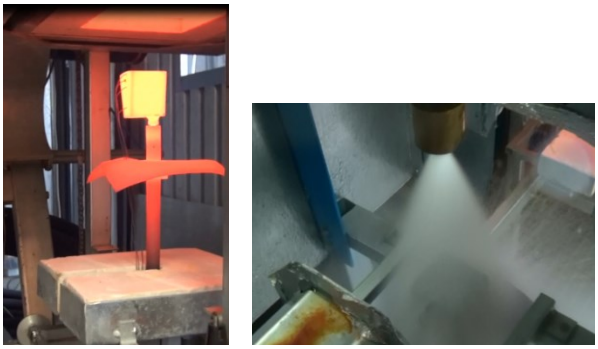

Figure 4 Photo of the test sample after removing from the furnace (left) and during cooling by the nozzle (right)

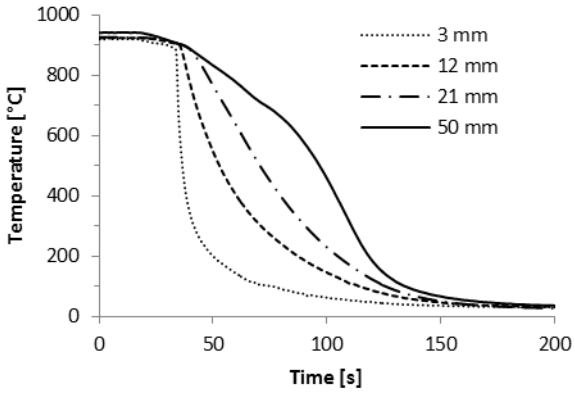

Figure 5 Measured temperatures (3, 12, 21 and 50 mm under the cooled surface)

Measured hardness and microstructure

The sample was cut after the cooling and the hardness and microstructure were measured in the axis of the sample. The quenching significantly increases hardness (Figure 6) and increases the content of the martensitic structure near the surface (Figure 7). The martensitic structure was observed to the depth 15 mm. The bainite, ferrite and pearlite were observed deeper in the material. The prediction of the CCT diagram with cooling curves is shown in Figure 8.

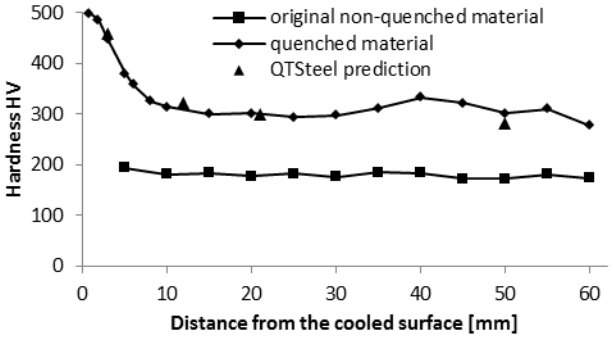

Figure 6 Measured hardness (quenched material - HV30, original material - HV 20) and prediction by the QTSteel software

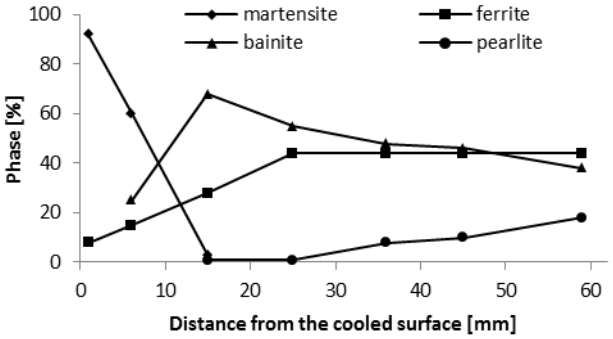

Figure 7 Measured phase composition

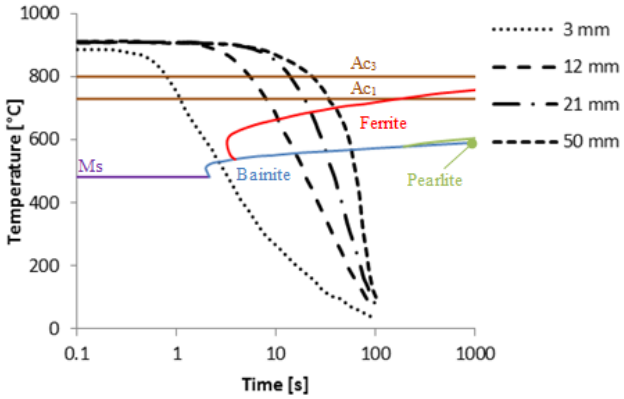

Figure 8 Predicted CCT diagram with cooling curves measured 3, 12, 21, 50 mm below outer surface

DESIGN OF THE COOLING SECTION

Based on previous measurement of nozzle cooling characteristics (HTC), the microstructure tests with small samples and numerical simulation of various cooling strategies, cooling section can be designed. The important factor which should be considered in the design of the cooling section is homogeneity of the cooling. Inhomogeneous cooling can lead to inhomogeneous material properties and deformation of the product.

The water distribution is the main factor which influences the cooling intensity and homogeneity. The example of

computed water distribution of the cooling unit (Figure 9) used for tube cooling is shown in Figure 10. The water distribution was computed by the software developed in the Heat Transfer and Fluid Flow Laboratory. The demonstration of possible design of the rail cooling unit is shown in Figure 11.

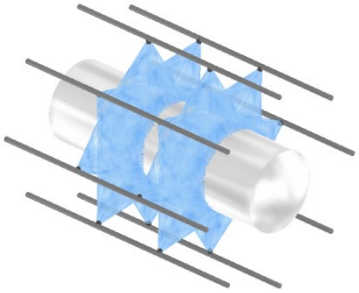

Figure 9 Visualisation of the cooling unit used for tube cooling

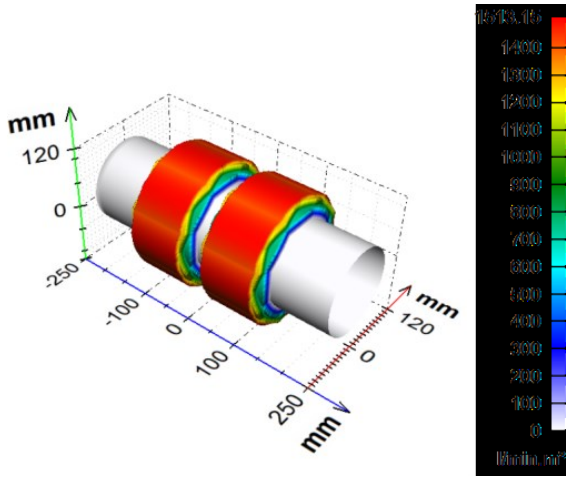

Figure 10 Computed water distribution of the cooling unit used for tube cooling

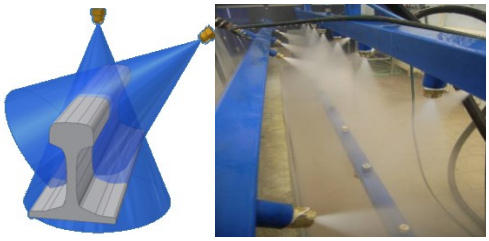

Figure 11 Laboratory cooling unit used for rail head heat treatment

FULL-SCALE EXPERIMENT

A laboratory test bench was designed for full-scale material samples [6, 7]. A piece of tube, rail, wire or plate of real dimensions is instrumented with thermocouples and the cooling is tested. The length of a laboratory test bench (Figure 12) is limited, hence the sample must be accelerated before entering to the tested cooling section to a velocity normally used in a plant, and after leaving the cooling section the direction of movement is reversed. In this way, the sample moves several times through the cooling section. This process of cooling is controlled to simulate running through the long cooling section used normally in the plant. Chosen nozzles, pressures, and header configurations are tested. The design of cooling section and the pressures used are modified until the demanded temperature regime is obtained. The full-scale material samples (Figure 13) are tested and then cut for tests of material properties and structures.

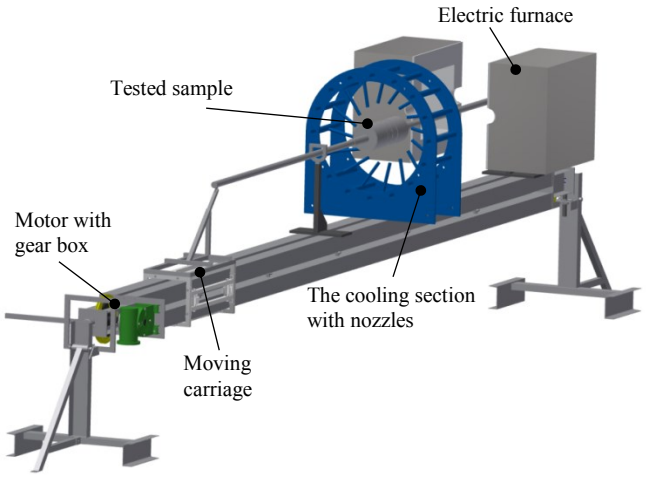

Figure 12 Laboratory test bench

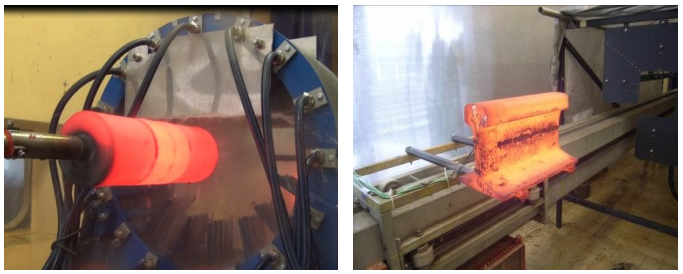

Figure 13 Samples of tube and rail running to the cooling section

CONCLUSION

The design of cooling sections used for heat treatment of long products is very extensive work. It utilizes numerical modelling, laboratory measurement and also pilot mill tests.

The first step is the search of the best cooling regime for steels for which this is not yet known. The second step is to obtain a selection of technical means in order to guarantee obtaining the prescribed cooling rates. Nozzle configurations and cooling parameters are selected and controllability of the cooling section is checked. The final step of the design is a laboratory test using a full size sample simulating plant cooling. Design based on laboratory measurement therefore minimizes the amount of expensive experimentation performed directly on the plant.

ACKNOWLEDGEMENT

"This work is an output of research and scientific activities of this project LO1202 with financial support from the MEYS under the programme NPU I"

REFERENCES

[1] Kotrbáček P., Horský J., Raudenský M., and Pohanka M., Experimental Study of Heat Transfer in Hot Rolling, *Revue de Metallurgie,* 2005, pp. 42-43

[2] Šimeček P., Turoň R., Hajduk D., Computer Model for Prediction of Mechanical Properties of Long Products after Heat Treatment, *68th Congress ABM 2013, Belo Horizonte, Brazil, 30.7.-2.8.2013*.

[3] Raudenský M., Heat transfer coefficient estimation by inverse conduction algorithm, *International Journal of Numerical Methods for Heat and Fluid Flow,* Vol. 3, No. 3, 1993, pp. 257-266.

[4] Pohanka M., and Horský J., Inverse algorithms for time dependent boundary reconstruction of multidimensional heat conduction model, *Thermophysics, 2007*, pp. 14-23. ISBN 978-80-227-2746-4.

[5]http://www.ita-tech.cz/en/products-services/heat-treatment/software-qtsteel

[6] Pohanka M., Bellerova H., and Raudenský M., Experimental Technique for Heat Transfer Measurements on Fast moving Sprayed Surfaces, *Journal of ASTM International,* Vol. 6, No. 4, *2009*.

[7] Raudensky M., Horsky J., Hajduk D., and Cecho L Interstand Cooling – Design, Control and Experience, *Journal of Metallurgical and Mining Industry,* Vol. 2, No. 3, 2010, ISSN 2075-0507.

OPTIMUM DIAMETER OF A CIRCULATING FLUIDISED BED COMBUSTOR WITH NEGATIVE WALL HEAT FLUX

Baloyi J. [*, 1, 2], Bello-Ochende T. [3] and Meyer J.P. [1]
[*]Author for correspence
[1]Department of Mechanical and Aeronautical Engineering, University of Pretoria, Private Bag X20, Hatfield, Pretoria, 0028, South Africa
[2]Modelling and Digital Science, Council for Scientific and Industrial Research, P.O. Box 395, Pretoria, 0001, South Africa
[3]Department of Mechanical Engineering, University of Cape Town, Private Bag X3, Rondebosch, 7701, South Africa
E-mail: jbaloyi@csir.co.za

ABSTRACT
The focus of the world is the reduction of greenhouse gases like carbon dioxide, which contribute to the global warming currently experienced. Since most of the carbon dioxide emitted into the atmosphere is from fossil fuel combustion, alternative energy source were developed and others are currently under study to see if they can be good alternatives. One of these alternative sources of energy is the combustion of wood instead of coal. Wood has an advantage for being a neutral carbon fuel source, and that currently installed infrastructure used to combust coal can be retrofitted to combust wood or a mixture of wood and coal in an attempt to reduce the carbon dioxide emissions. In this study the effect a change in diameter of a combustor has on irreversibilities in a 7 m circulating fluidised bed combustor with a negative wall heat flux, firing a mixture of air and solid pitch pine wood, was investigated. An analytical expression was derived that predicts the entropy generation rate, thereby the irreversibilities, of a combustor with a negative wall flux as a function of the combustor diameter. A numerical code was used to compute the molar fractions of combustion products needed as an input in the analytical expression. In the numerical code the combustion process was modelled by a non-premixed combustion model, with a P1 radiation model. Simulations were run using a steady Reynolds averaged Navier Stokes model. The analytical expression predicted the optimum diameter that results in minimum irreversibilities to be 0.32 m for a rich mixture with an Air-Fuel mass ratio of 6, and an incoming air temperature of 400 K.

INTRODUCTION
The focus of the world is the reduction of greenhouse gases like carbon dioxide. Since most of the carbon dioxide emitted into the atmosphere is from fossil fuel combustion, alternative energy source were developed and others are currently under study to see if they can make good alternatives. One of these alternative sources of energy is the combustion of wood instead of coal. Wood has an advantage for being a neutral carbon fuel source, and that currently installed infrastructure used to combust coal can be retrofitted to combust wood or a mixture of wood and coal in an attempt to reduce the carbon dioxide emissions

NOMENCLATURE

A	[mm^2]	Cross-sectional area
AF	[-]	Air-Fuel mass ratio
B_1	[-]	Equation term
B_3	[-]	Equation term
B_4	[-]	Equation term
B_6	[-]	Equation term
$\bar{c}$	[kJ/kmol.K]	Molar specific heat
c	[kJ/kg.K]	Specific heat
c_p	[kJ/kg.K]	Specific heat at constant pressure
C	[-]	Atomic carbon
C_d	[-]	One of the mixture fraction variance transport equation constant
C_g	[-]	One of the mixture fraction variance transport equation constant
CO	[-]	Carbon monoxide
CO_2	[-]	Carbon dioxide
D	[mm]	Combustor diameter
$\overline{f}$	[-]	Mixture fraction
$\overline{f'^2}$	[-]	Mixture fraction variance
$\vec{F}$	[-]	Body force
g	[m/s^2]	Gravitational acceleration magnitude
$\vec{g}$	[m/s^2]	Gravitational acceleration
G	[kg/s/m^2]	Mixture mass flux
$\overline{h}$	[kJ/kmol]	Specific enthalpy
$\overline{h}^0$	[kJ/kmol]	Enthalpy of formation

H	[mm] , [kJ]	Atomic hydrogen; Height; total enthalpy
H_2	[-]	Molecular hydrogen
H_2O	[-]	Water vapour
$\hat{i}$	[-]	Unit vector
$\dot{I}$	[W]	Irreversibility
k	[-]	Turbulent generate rate
L	[mm]	Length
$\dot{m}$	[kg/s]	Mass flow rate
M	[kg/kmol]	Molecular weight
n	[-]	Stoichiometric coefficient
N	[-]	Atomic nitrogen; Entropy generation number
N_2	[-]	Molecular nitrogen
O	[-]	Atomic oxygen
O_2	[-]	Molecular oxygen
P	[Pa]	Pressure
q''	[W/m^2]	Wall heat flux
$\overline{R}$	[kJ/kmol.K]	Universal gas constant
$\overline{s}$	[kJ/kmol.K]	Specific entropy
$\overline{s}^\circ$	[kJ/kmol.K]	Absolute entropy
$\dot{S}_{gen}$	[W/K]	Entropy generation rate
S_h	[-]	Viscous dissipation energy source term
S_m	[-]	Solid phase to gas phase mass transfer source term
T	[K]	Temperature
$\vec{v}$	[m/s]	Velocity
x	[-]	Molar fraction
X_1	[-]	Equation term
X_2	[-]	Equation term
X_3	[-]	Equation term
X_4	[-]	Equation term
Y	[-]	Mass fraction

Greek symbols

ρ	[kg/m^3]	Density
ε	[-]	Void fraction; turbulent dissipation rate
σ_t	[-]	One of the mixture fraction variance transport equation constant
μ	[Pa.s]	Molecular viscosity
μ_t	[Pa.s]	Turbulent viscosity
$\overline{\overline{\tau}}$	[-]	Stress tensor

Subscripts

0	[-]	Superficial
Air	[-]	Air
$char$	[-]	Char
CO	[-]	Carbon monoxide
CO_2	[-]	Carbon dioxide
f	[-]	Fuel
g	[-]	Gas
$gen,\min$	[-]	Minimum entropy generation rate
$gen(h)$	[-]	
$gen(p)$	[-]	Entropy generation rate due to frictional pressure drop
H_2	[-]	Molecular hydrogen
H_2O	[-]	Water vapour
$h-t$	[-]	Heat transfer
i	[-]	Counting index
l	[-]	Maximum number of products
m	[-]	Maximum number of reactants; mixture
mf	[-]	Minimum fluidisation
N_2	[-]	Molecular nitrogen
O_2	[-]	Molecular oxygen
p	[-]	Product species
r	[-]	Reactant species
ref	[-]	Environment reference
s	[-]	Solid species
sd	[-]	Dense zone solid species
se	[-]	Exit zone solid species
t	[-]	Total of solid and gas
th	[-]	Theoretical amount of air ratio
w	[-]	Wall

The influence of geometric parameters on the efficiency of energy production has been an area of interest for researchers looking to get the most out of their apparatus used for this purpose. Hua, Wu and Kumar [1] discovered that changing the wall conditions from adiabatic to heat loss through a wall on the combustion chambers has the effect of quenching, even extinguishing the combustion process inside the chamber burning a hydrogen-air mixture, as they vary from millimetre to micro scale size when they were analysed numerically. [2] expanded on the worked done in [1] to optimise the micro-combustor in terms of the best equivalence ratio to operate the micro-combustor at. Norton and Vlachos [3] numerically studied the effects of wall thickness and flow velocities on the combustion characteristics and flame stability in a premixed methane/air mixture micro-burner. They found two modes of flame blowout, one due to thick wall thermal conductivities and another due to low flow velocities. Louis et al [4 found that to compare well with experimental data it is necessary to include the mixing, combustion and heat loss associated with non-adiabatic modelling in accurately predicting the NO formation in flames with heat loss for an air cooled syngas combustion chamber. Li and Zhong [5] experimentally found that for a stainless steel micro-tube burning a methane/oxygen mixture the heat loss due radiation

constituted about 70% of the total heat loss. Feng, Liu and Li [6] found that the higher the axial wall temperature gradient the more stable the flame that can be realised for a given tube size when they numerically studied the combustion of an air-methane mixture inside a small tube. The technique of analysing and minimising the entropy generation rate of a process was demonstrated with good effect in studies by [7-10]. In furtherance of the work done in Baloyi, Bello-Ochende and Meyer [7], Baloyi, Bello-Ochende and Meyer [11] and [12] in this study the effect of a change in diameter of a combustor has on irreversibilities in a 7 m circulating fluidised bed combustor with a negative wall heat flux, firing a mixture of air and solid pitch pine wood, was investigated.

EXERGY ANALYSIS

The irreversibility generation rate that results from the combustion-heat transfer and frictional pressure drop processes taking place in an adiabatic combustor is as given by equation (1) [13-15].

$$\dot{I} = \frac{\dot{m}_f}{M_f}\left(\sum_{i=1}^{m} n_{ri}\left(\bar{h} - T_{ref}\bar{s}\right)_{ri} - \sum_{i=1}^{l} n_{pi}\left(\bar{h} - T_{ref}\bar{s}\right)_{pi}\right) - \left(1 - \frac{T_{ref}}{T_w}\right) q'' \pi D L \quad \textbf{(1)}$$

Since the wall temperature, the enthalpy and entropy terms of the combustion products are unkowns for a rich mixture in equation (1), the irreversibility generation rate can also be defined, by equation (2)

$$\dot{I} = T_{ref}\dot{S}_{gen} \quad \textbf{(2)}$$

Where $\dot{S}_{gen}$ is the entropy generation rate. The specific entropy is given by equation (3).

$$\bar{s}_{pi} = \bar{s}^{\circ}_{pi}(T) - \bar{R}\ln(Px_{pi}/P_{ref}) \quad \textbf{(3)}$$

The static pressure in the combustor is the same as the reference static pressure, i.e. $P = P_{ref}$, and the molar fraction of each product species, x_{pi}, is given by equation (4)

$$x_{pi} = n_{pi} \Big/ \sum_{i=1}^{l} n_{pi} \quad \textbf{(4)}$$

n_{pi} is the stoichiometric coefficient of combustion product species *i*. The same expressions apply for reactants. $\bar{h}$ is the specific enthalpy, $\bar{s}^{\circ}_{pi}$ is the absolute entropy, $\bar{R}$ is the universal gas constant, p is the static pressure, P_{ref} is the reference static pressure of the environment and T_{ref} is the reference temperature of the environment. . The specific entropy of the solid fuel was computed by defining [13] it as given by equation (5).

$$\bar{s} = \bar{c}\ln\left(T_f/298\right) \quad \textbf{(5)}$$

$\bar{c}$ is the molar specific heat of the solid fuel. The study was conducted a combustor with a negative heat flux wall condition burning pitch pine wood, and an incoming air temperature of 400 K as investigated in [11]. The combustor is as illustrated in Fig. 1. The combustor was made out of a cylinder with a negative heat flux wall condition, inlets for the solid fuel and primary air inlet for the air used to devolatilise the solid fuel and secondary air inlets that were needed to complete the combustion of the fuel.

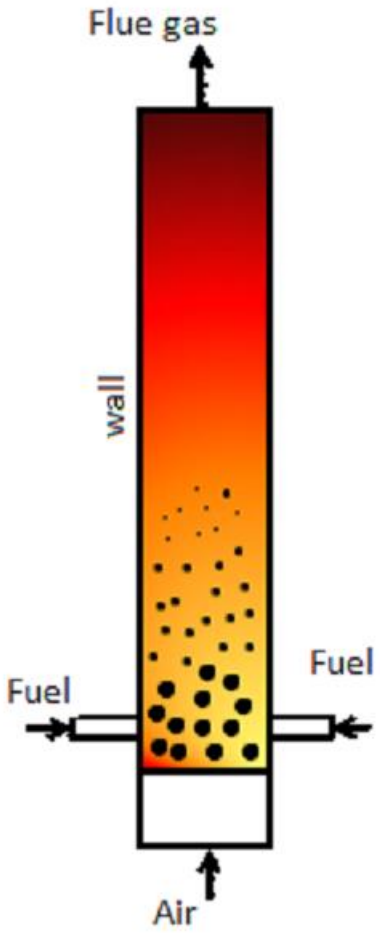

Figure 1 Schematic of a combustor (adapted from [7]).

The air-fuel mass ratio (AF) of 6 was chosen for this study because it was identified in [12] to be the minimum AF for a combustor with a negative heat

flux wall condition of 7500 W/m^2, and a diameter of 0.3 m as shown in Figure 2.

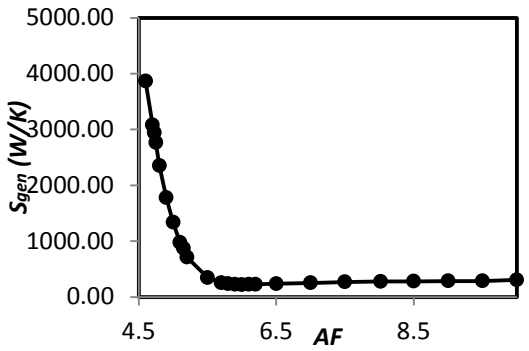

Figure 2 Plots of the variation of entropy generation rate with AF for case with wall heat flux of -7500 W/m^2.

The chemical formula of the solid fuel as computed in [11] is given by $C_{4.9}H_{7.2}O_2$, the lower heating value of the fuel from [11] was given as 16091.2 kJ/kg and the molecular weight of the fuel was calculated as 98 kg/kmol. The specific heat at constant pressure was also given as 1.680 kJ/kg.K. The entropy generation rate is constituted by the frictional pressure drop and combustion-heat transfer terms [16]. The frictional pressure drop term, due to the air-fuel mixture as it flows through the riser [17], was derived in [7] and is given by equation (6).

$$\dot{S}_{gen(p)} = \dot{m}_f\left(AF+1\right)\left(\rho_f-\rho_g\right)g\times \frac{\left[\begin{array}{l}\dfrac{\left(\varepsilon_{sd}-\varepsilon_{se}\right)\left(1-\varepsilon_{sd}\right)\dot{m}_f AF}{10\rho_g A} \\ +H_t\varepsilon_{sd} \\ +\ln\left(\dfrac{\varepsilon_{se}-\varepsilon_s^*}{\varepsilon_{sd}-\varepsilon_s^*}\right)\left(\dfrac{\varepsilon_{sd}-\varepsilon_s^*}{10\rho_g A}\right)\left(1-\varepsilon_{sd}\right)\dot{m}_f AF\end{array}\right]}{\left(\varepsilon_{se}\rho_f+\left(1-\varepsilon_{se}\right)\rho_g\right)T_m} \quad \textbf{(6)}$$

ΔP is the pressure drop across the combustor, $\dot{m}_f$ is the solid fuel mass flow rate, ρ_m is the mixture density, T_m is the mixture temperature.

The combustion-heat transfer term, due to combustion and/or heat transfer processes, was also derived in [7] and is given by equation (7).

$$\dot{S}_{gen(h)} = \frac{\dot{m}_f}{M_f}\left(\begin{array}{l}\displaystyle\sum_{j=1}^{l} n_{pj}\left(\bar{s}^\circ-\bar{R}\ln\left(x\right)\right)_{Pj} \\ \displaystyle-\sum_{j=1}^{m} n_{rj}\left(\bar{s}^\circ-\bar{R}\ln\left(x\right)\right)_{rj} \\ \dfrac{\rho_{char}}{\rho_g}n_{char}c_{char}M_{char}\ln\left(T_{char}/298\right) \\ -\dfrac{\rho_f}{\rho_g}n_f c_f M_f\ln\left(T_f/298\right)\end{array}\right) \quad \textbf{(7)}$$

A negative wall heat flux of 7500 W/m^2 was applied over the wall of the combustor, which results in a heat rate of energy extracted through the wall of 48.5 kW$_{th}$. This corresponds to about 20% of the total thermal heat rate of 241 kW$_{th}$ generated in the combustor for a fuel mass flow rate of 0.015 kg/s. The analysis of the entropy generation rate is the same as that of [7] except that there is an additional term due to heat transfer [16] through the wall of the combustor, and this term is as expressed in equation (8).

$$\dot{S}_{gen(h-t)} = -\frac{2\pi LDq''}{T_m+\Delta T} \quad \textbf{(8)}$$

Where L is the length of the combustor, D is the diameter of the combustor, q'' is the wall heat flux and ΔT is the change if temperature across the length of the combustor. The only term that is unknown in equation (8) is ΔT which can be described by equation (9).

$$\Delta T = \frac{q''}{c_p GSt} \quad \textbf{(9)}$$

Where $G = \dot{m}_f\left(AF+1\right)/A$ is the mixture mass flux and $St = Nu/\mathrm{Re}_D\,\mathrm{Pr}$ is the Stanton number. The Prandtl number Pr is assumed to be 0.69 [18] for the gas species mixture involved in the combustion process and Re_D is the Reynolds number based on the combustor diameter. The Nusselt number [16] is given by equation (10), assuming turbulent internal flow.

$$Nu = 0.023\,\mathrm{Re}_D^{\,0.8}\,\mathrm{Pr}^{0.4} \quad \textbf{(10)}$$

Substituting equation (10) into equation (9) and taking all the above into consideration, equation (9) becomes:

$$\Delta T = \frac{\pi D^2 q''}{0.1148 c_p \dot{m}_f (AF+1)\mathrm{Re}_D^{-0.2}} \quad \textbf{(11)}$$

Substituting equation (11) into equation (8) results in:

$$\dot{S}_{gen(h-t)} = -\frac{0.2296\pi L D c_p \dot{m}_f (AF+1) q'' \mathrm{Re}_D^{-0.2}}{0.1148 c_p \dot{m}_f (AF+1) T_m \mathrm{Re}_D^{-0.2} + \pi D^2 q''} \quad \textbf{(12)}$$

When equation (12) is added to equation (7), what results is an equation that describes the entropy generation rate due combustion and heat transfer through a wall for the combustor with a heat flux wall condition, as expressed by equation (13).

$$\dot{S}_{gen} = \frac{\dot{m}_f}{M_f}\begin{pmatrix} \sum_{j=1}^{l} n_{pj}\left(\bar{s}^\circ - \bar{R}\ln(x)\right)_{Pj} \\ -\sum_{j=1}^{m} n_{rj}\left(\bar{s}^\circ - \bar{R}\ln(x)\right)_{rj} \\ +\frac{\rho_{char}}{\rho_g} n_{char} c_{char} M_{char} \ln\left(T_{char}/298\right) \\ -\frac{\rho_f}{\rho_g} n_f c_f M_f \ln\left(T_f/298\right) \end{pmatrix} - \frac{0.2296\pi L D c_p \dot{m}_f (AF+1) q'' \mathrm{Re}_D^{-0.2}}{0.1148 c_p \dot{m}_f (AF+1) T_m \mathrm{Re}_D^{-0.2} + \pi D^2 q''} \quad \textbf{(13)}$$

Where the Reynolds number is as expressed by equation (14).

$$\mathrm{Re}_D = \frac{4\dot{m}_f (AF+1)}{\pi \mu D} \quad \textbf{(14)}$$

Where μ is the mixture dynamic viscosity.

When taking the all the terms that constitute the entropy generation rate into account by adding equation (13) with equation (6), the total entropy generation rate is expressed by equation (15).

$$\dot{S}_{gen} = B_1\left[\frac{X_1}{\pi D^2} + B_3 + \frac{4X_2}{\pi D^2}\right] + B_4 - \frac{X_3 D \mathrm{Re}_D^{-0.2}}{B_6 \mathrm{Re}_D^{-0.2} + X_4 D^2} \quad \textbf{(15)}$$

Where

$$B_1 = \frac{\dot{m}_f (AF+1)(\rho_f - \rho_g) g}{\left[\varepsilon_{se}\rho_f + (1-\varepsilon_{se})\rho_g\right] T_m} \quad \textbf{(16)}$$

$$B_3 = H_t \varepsilon_{sd} \quad \textbf{(17)}$$

$$B_4 = \dot{S}_{gen(h)} = \frac{\dot{m}_f}{M_f}\begin{pmatrix} \sum_{j=1}^{l} n_{pj}\left(\bar{s}^\circ - \bar{R}\ln(x)\right)_{Pj} \\ -\sum_{j=1}^{m} n_{rj}\left(\bar{s}^\circ - \bar{R}\ln(x)\right)_{rj} \\ +\frac{\rho_{char}}{\rho_g} n_{char} c_{char} M_{char} \ln\left(T_{char}/298\right) \\ -\frac{\rho_f}{\rho_g} n_f c_f M_f \ln\left(T_f/298\right) \end{pmatrix} \quad \textbf{(18)}$$

$$B_6 = 0.1148 c_p \dot{m}_f (AF+1) T_m \quad \textbf{(19)}$$

$$X_1 = \frac{(\varepsilon_{sd} - \varepsilon_{se})(1-\varepsilon_{sd})\dot{m}_f AF}{10\rho_g} \quad \textbf{(20)}$$

$$X_2 = \frac{\dot{m}_f AF}{10\rho_g} \ln\left(\frac{\varepsilon_{se} - \varepsilon_s^*}{\varepsilon_{sd} - \varepsilon_s^*}\right)(\varepsilon_{sd} - \varepsilon_s^*)(1-\varepsilon_{sd}) \quad \textbf{(21)}$$

$$X_3 = 0.2296\pi L c_p \dot{m}_f (AF+1) q'' \quad \textbf{(22)}$$

$$X_4 = \pi q'' \quad \textbf{(23)}$$

The entropy generation rate in equation (15) can be expressed as a function of Reynolds number as given by equation (24).

$$\dot{S}_{gen} = \left[\frac{\pi B_1 X_1 \mu^2}{4\dot{m}_f^2 (AF+1)^2} + \frac{\pi B_1 X_2 \mu^2}{4\dot{m}_f^2 (AF+1)^2}\right]\mathrm{Re}_D^2 + B_1 B_3 + B_4 - \frac{4\pi\mu X_3 \dot{m}_f (AF+1)\mathrm{Re}_D^{0.8}}{\pi^2 \mu^2 B_6 \mathrm{Re}_D^{1.8} + 16 X_4 \dot{m}_f^2 (AF+1)^2} \quad \textbf{(24)}$$

The entropy generation number, N_s [7] which is the quotient of the entropy generation rate at any Reynolds number and the minimum entropy generation rate, was used to analyse the penalty paid by running the combustor at a Reynolds

number other than the optimum and is as given by equation (25).

$$N_s = \frac{\dot{S}_{gen}}{\dot{S}_{gen,\min}} \qquad \textbf{(25)}$$

NUMERICAL MODEL

The combustor produced 241 kW_{th} when complete combustion of pitch pine wood occurs with theoretical amount of air. The combustor had a diameter of 300 mm and a height of 7000 mm as illustrated in Fig. 3.

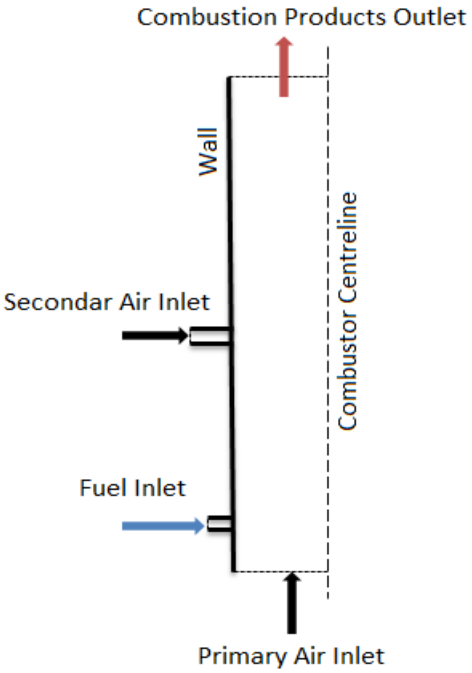

Figure 3 Schematic of the combustor showing boundary placements (adapted from [7]).

The mass flow rate of the incoming solid fuel was fixed at a value of 0.015 kg/s so as to have a common maximum heat generation rate of 241 kW_{th} since the lower heating value is fixed and unique for any particular fuel. ANSYS Fluent 14 [19] was used to simulate the combustion process inside the combustor. The combustion process was modelled using the non-premixed combustion model because the solid fuel is only specified in ultimate analysis data [20] as given in Table 2, and the combustion model gives an option of specifying the fuel as an empirical stream. The inlet diffusion option was selected.

Table 1 Pitch pine ultimate analysis data (adapted from [19]).

Element	Value
C	59.0 (%)
H	7.2 (%)
O	32.7 (%)
Ash	1.13 (%)
HHV	24220 (kJ/kg)
LHV	16091.2 (kJ/kg)
Molecular weight	98 (kg/kmol)

The continuity and momentum equations [19] as expressed by equation (26) and equation (28) respectively were solved for under steady state condition.

$$\nabla \cdot \left(\rho \vec{v} \overline{f}\right) = \nabla \cdot \left(\frac{\mu_t}{\sigma_t} \nabla \overline{f}\right) + s_m \qquad \textbf{(26)}$$

$$\nabla \cdot \left(\rho \vec{v} \overline{f'^2}\right) = \nabla \cdot \left(\frac{\mu_t}{\sigma_t} \nabla \overline{f'^2}\right) + C_g \mu_t \left(\nabla \overline{f}\right)^2 - C_d \rho \frac{\varepsilon}{k} \overline{f'^2} \qquad \textbf{(27)}$$

$$\nabla \cdot \left(\rho \vec{v} \vec{v}\right) = -\nabla p + \nabla \cdot \left(\bar{\bar{\tau}}\right) + \rho \vec{g} + \vec{F} \qquad \textbf{(28)}$$

The stress tensor [19] is given by equation (29).

$$\bar{\bar{\tau}} = \mu \left[\left(\nabla \vec{v} + \nabla \vec{v}^T\right) - \frac{2}{3} \nabla \cdot \vec{v} \hat{i}\right] \qquad \textbf{(29)}$$

μ is the molecular viscosity of the continuous phase, $\vec{F}$ is the interactive body forces between the dispersed and the continuous phases, S_m is the source term accounting for the mass transfer from the solid phase to the gas phase and $\hat{i}$ is a unit vector. $\overline{f}$ and $\overline{f'^2}$ are the mixture fraction and its variance, and are computed by applying an assumed shape probability density function (β-function) when modelling the turbulence-chemistry interaction.

The energy for the non-premixed combustion model [19] was as expressed by equation (30).

$$\nabla \cdot \left(\rho \vec{v} H\right) = \nabla \cdot \left(\frac{k_t}{c_p} \nabla H\right) + S_h \qquad \textbf{(30)}$$

The total enthalpy H is given by equation (31).

$$H = \sum_{j=1}^{m} Y_j \int_{T_{ref,j}}^{T} \left(c_{p,j} dT + h_j^0 \left(T_{ref,j}\right)\right) \qquad \textbf{(31)}$$

Y_j is the mass fraction, $c_{p,j}$ is the specific heat and constant pressure and $h_j^0\left(T_{ref,j}\right)$ is the enthalpy of

formation of the j^{th} species. S_h is the source term due to viscous dissipation. The use of the chosen combustion model required the use of a turbulent model because the combustion model is a mixture model. To this end the $k-\varepsilon$ turbulent model with enhanced wall function option was chosen for all simulations.

The combustor had four mass flow inlets for the solid fuel as shown in Figure 4, each with equal mass flow rate of 0.00375 kg/s. The inlet temperature of the fuel at each inlet was set at 600K. The temperature value was selected to be same as the devolatilisation temperature of pitch pine [20]. The oxidising air was split into the primary and secondary air, each making up half of the total air used in the oxidation of the fuel. The reason for splitting the oxidising air was to enable the modelling of incomplete combustion to take place. The primary air entered the combustor at the base with a single fixed mass inlet, with half of the total air mass flow rate. The secondary air four fixed mass inlets were situated a quarter of the height up the combustor, each having an eighth of the total air mass flow rate. The inlet temperature at all eight air inlets was set at 400K. The wall boundar condition of the combustor was a negative heat flux of 7500 W/m^2. The data that was extracted from the simulations were the temperature at the pressure outlet boundary and the combustion products molar fractions. Figure 4 shows the placement and types of boundaries applied on the combustor.

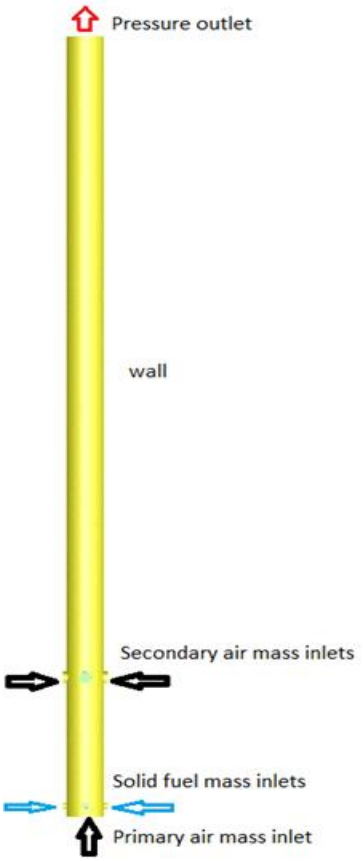

Figure 4 Schematic of the geometry used in Ansys Fluent 14 to model the combustor.

The mesh used for the numerical simulations aried from 750000 to 850000 unstructured polyhedral cells. The Presto scheme was used to solve for pressure and second-order upwind schemes were used to solve for the continuity, energy, turbulence and mass fraction. The results obtained when using equation (6) and equation (7) to process data from numerical simulations and data from thermodynamics tables data [13] were compared for the case of complete combustion with varying amount of excess air, that is lean mixtures. It was found that the results from numerical simulations data compared well with results from thermodynamics tables data as shown in Figure 5.

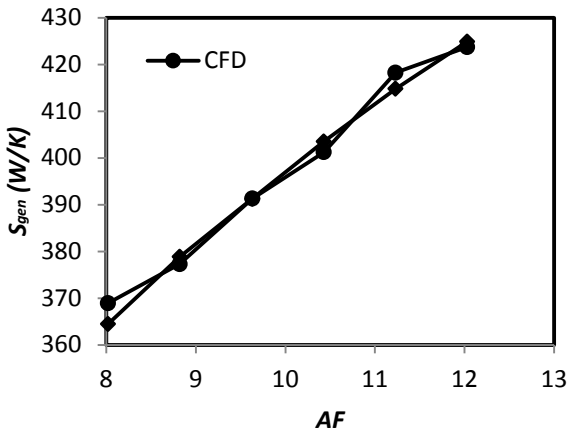

Figure 5 The entropy generation rate profile as a function of AF in an adiabatic combustor for lean mixtures.

RESULTS AND DISCUSSION

The molar fractions of combustion products were incorporated into equation (24) in order to compute the entropy generation rate of the combustor. The computed entropy generation rate for a wide range of Reynolds number based on the combustor diameter was plotted in Figure 6. The figure shows that the minimum entropy generation rate of about 218 W/K occurred at a Reynolds number of about 25000. This Reynolds number corresponds to a combustor diameter of 0.32 m as shown by Figure 7. Since the AF has been fixed at a value of 6, the entropy generation rate term due to combustion remains constant even when the there is a change in combustor diameter. Also given that the contribution of the pressure loss term is negligible as discovered in [7], therefore all the change in entropy generation rate is all due to the heat transfer term through the wall of the combustor. This means that the optimum diameter discovered in this study is unique for a combustor run at an AF of 6.

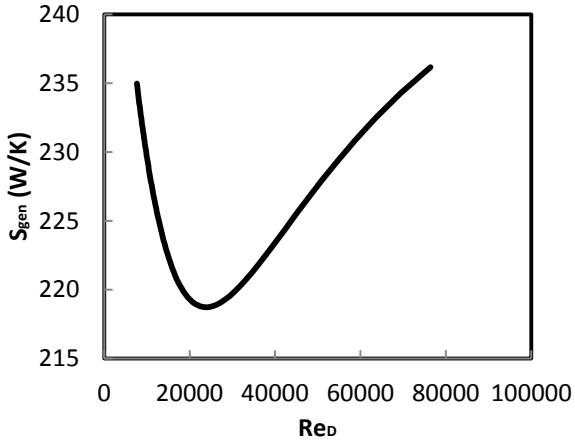

Figure 6 The entropy generation rate profile as a function of Re_D in a combustor ran at an AF of 6.

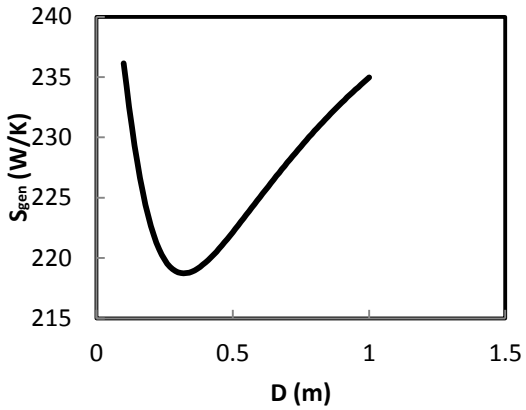

Figure 7 The entropy generation rate profile as a function of combustor diameter in a combustor ran at an AF of 6.

The corresponding irreversibilities rate was also computed, and is shown in Figure 8.

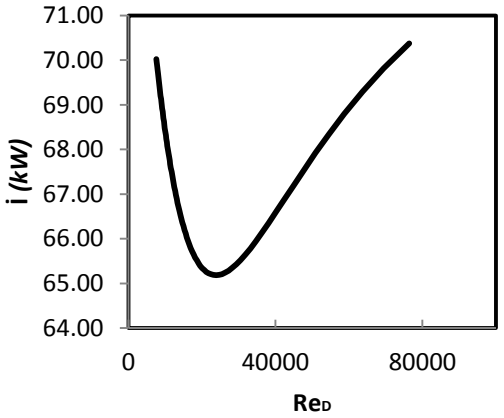

Figure 8 The irreversibilities rate profile as a function of Re_D in a combustor ran at an AF of 6.

The penalty that is paid when a combustor has a diameter that is not 0.32 was also computed as represented by N_s as can be seen in Figure 9. The figure shows that at diameters of 0.1 m and 0.97 the penalty paid was an extra 7% in entropy generation rate.

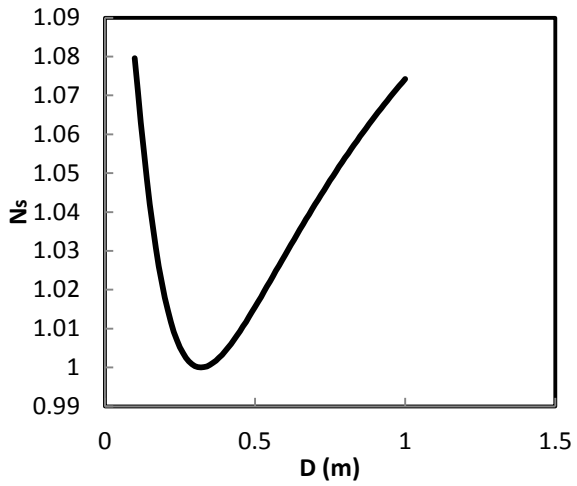

Figure 9 The entropy generation number profile as a function of combustor diameter in a combustor ran at an AF of 6.

CONCLUSIONS

The combustor with a negative heat flux wall condition was simulated at an AF of 6 for varying combustor diameters to find the diameter with the minimum entropy generation rate. It was discovered that a diameter of 0.32 m resulted in the minimum entropy generation rate. It was also discovered that the penalty paid, when a combustor with a diameter of 0.1 m or 0.97 m was used, was 7%

ACKNOWLEDGEMENTS

The authors would like express their appreciation to the National Research Foundation (NRF), University of Pretoria and the Council for Scientific and Industrial Research (CSIR) for the financial support and making their infrastructures available for this study.

REFERENCES

[1] Hua J, Wu M, Kumar K. Numerical simulation of the combustion of hydrogen-air mixture in micro-scaled chambers. Part I: Fundamental study. Chemical Engineering science 2005; 60: 3497-3506.
[2] Hua J, Wu M, Kumar K. Numerical simulation of the combustion of hydrogen-air mixture in micro-scaled chambers. Part II: CFD analysis for a micro-combustor. Chemical Engineering science 2005; 60: 3507-3515.
[3] Norton DG, Vlachos DG. Combustion characteristics and flame stability at the microscale: a CFD study of premixed methane/air mixtures. Chemical Engineering science 2003; 58: 4871-4882.
[4] Louis JJJ, Kok JBW, Klein SA. Modeling and measurements of a 16-kW turbulent nonadiabatic syngas diffusion flame in a cooled cylindrical combustion chamber. Combustion and Flame 2001; 125: 1012-1031.
[5] Li J, Zhong B. Experimental investigation on heat loss and combustion in methane/oxygen micro-tube combustor. Applied Thermal Engineering 2008; 28: 707-716.
[6] Feng L, Liu Z, Li Y. Numerical study of methane and air combustion inside a small tube with an axial temperature gradient at the wall. Applied Thermal Engineering 2010; 30: 2804-2807.
[7] Baloyi J, Bello-Ochende T, Meyer JP. Thermodynamic optimisation and computational analysis of irreversibilites in a small-scale wood-fired circulating fluidised bed adiabatic combustor. Energy 2014; 70: 653-663.
[8] Le roux WG, Bello-Ochende T, Meyer JP. Optimum performance of a small-scale open and direct solar thermal Brayton cycle at various environmental conditions and constraints. Energy 2012; 46 (1): 42-50.
[9] Mwesigye A, Bello-Ochende T, Meyer JP. Numerical investigation of entropy generation in a parabolic through receiver at different concentration ratios. Energy 2013; 53: 114-127.
[10] Le Roux WG, Bello-Ochende T, Meyer JP. Operating conditions of an open and direct solar thermal Bryaton cycle with optimised cavity receiver and recuperator. Energy 2011; 36 (10): 6027-6-36.
[11] Baloyi J, Bello-Ochende T, Meyer JP. "The analysis of exergy destruction of a wood fired adiabatic combustor". International Conference on Applied Energy. Pretoria, South Africa, 2013.
[12] Baloyi J, Bello-Ochende T, Meyer JP." Wall heat flux and air inlet temperature influences on the thermodynamic optimisation of irreversibilities of a small scale circulating fluidised bed combustor". manuscript, 2015.
[13] Moran MJ, Shapiro HN. Fundamentals of engineering thermodynamics. 3rd Ed., SI Version, John Wiley and Sons Inc.: Chichester, 1998.
[14] Anamalai K, Puri K. Advanced thermodynamics engineering. CRC Press Inc.: Florida, 2002.
[15] Bejan A. Advanced engineering thermodynamics. John Wiley and Sons Inc.: New York, 1988.
[16] Bejan A. Entropy generation minimization: The method of thermodynamic optimization of finite-size systems and finite-time processes. CRC Press Inc.: Florida, 1996.
[17] Kunii D, Levenspiel O. Fluidization Engineering. Stoneham: Massachusetts, 1991.

[18] White FM. Viscous Fluid Flow. 3rd Ed., International Edition. McGraw-Hill: Singapore, 2006.
[19] ANSYS FLUENT Release 14.0. Theory Guide. ANSYS Inc.: Southpointe, 2011.
[20] Tillman DA, Rossi AJ, Kitto WD. Wood Combustion: Principles, Processes and Economics. Academic Press Inc.: New York, 1981.

DIMENSIONLESS PARAMETERS FOR A FREE PISTON STIRLING REFRIGERATOR

Heidrich, J.W.F. and Prata, A.T.*
*Author for correspondence
Department of Mechanical Engineering
Federal University of Santa Catarina
88.040-900 Florianoolis, SC
Brazil
E-mail: prata@polo.ufsc.br

ABSTRACT

The present work investigates the dimensionless parameters associated to the operation of a free piston Stirling refrigerator. Stirling refrigeration cycles are found in some applications such as low operating temperature coolers, medical diagnostic equipments and sophisticated electronics (superconductivity components and devices). More recently, Stirling refrigerators are also being proposed for domestic applications, as an alternative for conventional hermetic compressors and vapor compression cycles. In what follows, a computational model explores the working gas thermodynamic behavior and evaluates the performance of the Stirling cooler components. To simulate the working fluid behavior inside the chambers, use is made of a global thermodynamic model, and to model the heat exchanger and the regenerator a discretized approach is adopted using the finite volume methodology. Dynamic equations are used to simulate the solid moving parts composed by the piston, displacer, and springs. An electric circuit represented the linear electric motor and its components. From the governing equations that describe the performance of the Stirling refrigerator, dimensionless parameters are identified and interpreted. From a sensitivity analysis the most critical parameters are determined and the optimum operational condition is explored. The advantage of presenting the Stirling performance in terms of the dimensionless parameters is discussed, allowing different sizes of refrigerators to be considered.

INTRODUCTION

Stirling engines and refrigerators are known since the nineteenth century [1] and recent advances have pushed its applications to a diversity of areas including domestic refrigeration [2]. Stirling refrigerators are reciprocating machines in which the working fluid is a pressurized gas such as helium. Figure 1 presents a schematic view of the β-configuration linear free piston Stirling refrigerator employed in the present work. As shown, the basic parts are the electric motor, springs, piston, displacer, regenerator, the hot and cold chambers, and the hot and cold heat exchangers. The working fluid is shuttled between hot and cold chambers by means of a displacer and the change in temperature experienced by the gas is provided by the oscillating movement of a piston that converts the pressure wave (mechanical energy) into a temperature wave (thermal energy). The pressure and temperature variations are of constant amplitude and the period depends on the electrical frequency of a driven electric motor. A key feature of the Stirling refrigerator in particular and of the Stirling machine in general is the resonance frequency of the thermal pendulum. The electric motor drives the piston that compresses and expands the gas inside the chambers, and the springs (one attached to the piston and the other to the displacer) allow the operation at the resonance frequency.

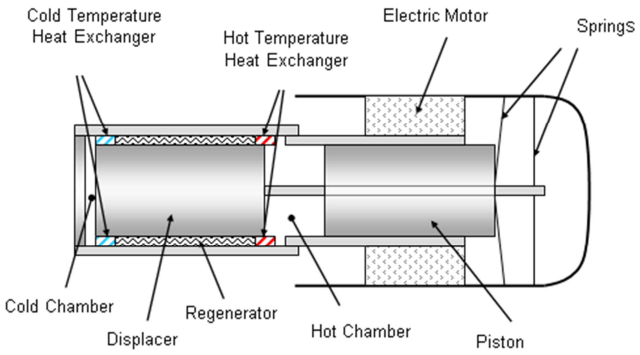

Figure 1 Schematic view of the Stirling refrigerator employed in the present work

Referring do Figure 1, as the piston moves to the left, the gas volume is decreased and the gas temperature is increased. The piston displacement to the left also causes the displacer displacement to the right, which tends to push the gas from the hot chamber to the hot heat exchanger. Thus, the displacer is responsible for moving the gas from the chambers to the heat exchangers. The piston is free to move with respect to the rod, which is attached at its left to the displacer, and at its right to one of the springs (the other spring is attached to the piston). Pressure in both chambers tend to be uniform throughout the entire cycle and the difference in area at the left and right sides of the displacer, caused by the rod cross sectional area, creates a resultant force in it which points to the right when the piston moves to the left and vice versa. The regenerator storage the thermal energy during the operation of the cycle and acts as a

thermal barrier between the hot and cold ends of the machine. When the working gas is displaced from the hot to the cold chamber, due to the displacer movement, heat is transferred from the gas to the regenerator and thermal energy is temporarily stored in the regenerator matrix. When the working gas is displaced from the cold to the hot end of the machine, the stored thermal energy is released from the regenerator matrix to the gas. Piston and displacer lubrication is performed aerostactically, using the gas itself.

MATHEMATICAL MODEL

Considerable work has been performed on the cycle analysis of the Stirling machine. Examples include [3-8]. More recently [9], a non-linear mathematical analysis was conducted for a α-configuration Stirling refrigerator which included dimensionless parameters. The present investigation differs from the previous one for presenting a detailed analysis of variables such as pressure, velocity, temperature, and density, along the regenerator and as a function of time. Pressure drop and heat transfer within and along the regenerator allow for a more realistic condition and permit the influence of the regenerator thermal conductivity, heat capacity and density on the refrigerator performance to be evaluated. Furthermore, the full dynamics of piston and displacer are taken into account, together with the performance of the linear electric motor.

The thermodynamic properties of the working fluid are assumed to be uniform inside the hot and cold chambers, varying only with time. Ignoring kinetic and potential contributions, the energy equation for the gas inside the chambers can be written as

$$\dot{Q} + \dot{W} + \dot{m}_i h_i = \dot{m}_o h_o + d(me)/dt \qquad (1)$$

where $\dot{m}$ is the mass flow rate going in or out of the chamber, h is enthalpy and e is internal energy. The chambers are taken adiabatic, that is, $\dot{Q} = 0$, and the mechanical power is given by

$$\dot{W} = -pdV/dt \qquad (2)$$

Mass conservation for the gas inside the chambers are expressed by

$$dm/dt = \dot{m}_o - \dot{m}_i \qquad (3)$$

and mass flow rate going in or out of the chambers is determined from the average velocity through the regenerator which is function of the pressure at its hot and cold extremes.

The heat exchanger employed in the present configuration is a metallic strip folded in several layers to form a corrugated structure that can be approximated by a stack of parallel plate channel, as seen in Figure 2. The gas temperature distribution along the flow direction, x, was obtained from

$$\dot{m} c_p dT_g/dx = h_{ex} P[T_w(x) - T_g(x)] \qquad (4)$$

where T_g and T_w are, respectively, the gas and the wall temperature at a particular streamwise location; h_{ex} is the heat transfer coefficient and P is the overall perimeter. The channel wall temperature, T_w, depends on the external temperature of the heat exchanger and on the conduction mechanism along its parts. In the present model the external temperature of both heat exchangers will be prescribed (T_H and T_C for the hot and cold reservoir, respectively), and the channel wall temperature will be taken as an average between those temperatures and the gas temperature.

At a given time the local mass flow rate $\dot{m}$ along the heat exchanger is taken to be constant. From its value and the overall gas temperature difference between entrance and exit, the instantaneously heat transfer at each heat exchanger can be obtained.

The regenerator in the present work is a plastic strip wrapped in spiral form around the cylinder shape shown in Figure 2. The volume occupied by the gas in the regenerator is of the same order of magnitude of that in the chambers and the gas is subjected to density variations along the working cycle. Within the regenerator the flow is considered to be two dimensional and compressible between two parallel plates; curvature effects are negligible and can be disregarded since the average radius of curvature of the plates is of the order of 0.1m and the distance between two plates is of the order of 0.0001m.

Conservation of mass and momentum for the gas inside the regenerator can be written as, respectively,

$$\frac{\partial \rho}{\partial t} + \frac{\partial(\rho u)}{\partial x} = 0 \qquad (5)$$

$$\rho \frac{\partial u}{\partial t} + \rho u \frac{\partial u}{\partial x} = -\frac{dp}{dx} + \frac{4}{3}\mu \frac{\partial^2 u}{\partial x^2} - 12\mu \frac{u}{a^2} \qquad (6)$$

where u is the local velocity component along the flow direction integrated over the cross sectional area of the channel, and a is the channel height. The right most term on the second equation represents the viscous contribution that is obtained under the assumption of a parabolic velocity profile within the channel, which is a laminar assumption justified due to the small Reynolds number encountered between the channel walls. It should be noted that u varies with time and along the longitudinal direction. To obtain the overall mass flow rate through the regenerator at a particular axial location, the local mass flow rates at each channel are added up considering that density, average velocity and area are the same for all channels.

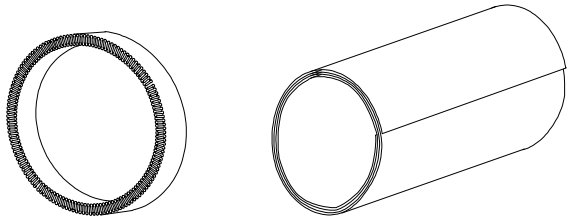

(a) (b)

Figure 2 Schematic view of (a) heat exchanger and (b) regenerator

The density variation with temperature and pressure requires that the energy equation for the gas should also be considered. For a compressible one-dimensional flow, the temperature within the regenerator satisfies the following equation,

$$c_v aW \frac{\partial(\rho T_g)}{\partial t} + c_p \frac{\partial(\dot{m} T_g)}{\partial x} = \\ = h_{reg} W([T_{reg}(x) - T_g(x)] \quad (7)$$

where W is the total width of the plastic strip employed in the regenerator, $\dot{m}$ is the local mass flow rate, and T_{reg} is the regenerator wall temperature at a given location obtained from the following conduction equation

$$\rho_{reg} c_{reg} \frac{\partial(T_{reg})}{\partial t} = k_{reg} \frac{\partial^2(T_{reg})}{\partial x^2} + \\ + \frac{h_{reg}}{b}([T_g(x) - T_{reg}(x)] \quad (8)$$

in which b is the thickness of the plastic strip.

Equations (5) to (8), in addition to the ideal gas law, form a complete the set of five equations required to calculate ρ, u, p, T_g, and T_{reg}. Those equations are discretized and solved numerically following the finite volume methodology [11].

The linear electrical motor is modeled assuming a simplified electric circuit where the resistance, R, the inductance, L, and the actuator voltage, V_m, are in series and fed by an electric voltage, V,

$$V = Ri + L\, di/dt + V_m \quad (9)$$

where i is the electric current through the motor. The actuator voltage can be written as,

$$V_m = \alpha\, dx_p/dt \quad (10)$$

in which x_p is the instantaneous piston location, and α is the actuator constant. The magnetic force, F_m, that drives the piston is obtained from, $F_m = i\alpha$. To obtain full benefit from the mechanical energy generated by the motor, the magnetic force should be in phase with the piston displacement.

Ignoring spring damping, the piston and displacer equations can be written as

$$F_p = k_p x_p + m_{p+a} \ddot{x}_p \quad (11)$$

$$F_d = k_d x_d + m_d \ddot{x}_d \quad (12)$$

where F is the resultant force, k is the spring stiffness, m is mass, and x is the location; subscripts p and d apply for the piston and displacer, respectively; m_{p+a} is the mass for the piston and actuator and m_d is the displacer mass.

The resultant forces acting on the piston and actuator, respectively, are

$$F_p = F_m - p_h(A_p - A_r) + p_o(A_p - A_r) \quad (13)$$

$$F_d = -p_c A_d + p_h(A_d - A_r) + p_o A_r \quad (14)$$

where A_p, A_d and A_r are, respectively, the areas of piston, displacer, and rod, and p_c, p_h, and p_o are, respectively, the pressure in the cold and hot chamber, and the pressure at the back chamber. The back chamber is located behind the springs and remains at a constant pressure along the operating cycle, equal to the cycle average pressure. The working gas inside the back chamber has a small influence on the refrigerator performance.

Equations (11) and (12) allow the calculation of the piston and displacer locations as a function of time once the thermodynamic and fluid flow quantities have been determined. The mathematical model described here was first explored in [10], where details about the solution methodology can be found. In [10] the model was employed to investigate a Stirling refrigerator having a cooling capacity of 100 W. The chosen machine and operation conditions were used to explore the thermodynamic properties of the gas during a working cycle, as well as the heat and fluid flow at the different parts of the refrigerator. Comparisons with experiments indicated consistence of the physical assumptions adopted.

DIMENSIONLESS EQUATIONS

In writing the dimensionless equations for the present investigation the fluid temperature exiting the hot and cold heat exchangers was taken as the corresponding temperature of the heat reservoir, that is, either T_H or T_C, respectively. That avoided the solution of equation (4) allowing the instantaneous heat transfer in the heat exchangers to be determined as

$$\dot{Q}_C = \dot{m} c_p (T_g - T_C) \text{ and } \dot{Q}_H = \dot{m} c_p (T_g - T_H) \quad (15)$$

A further simplification for the dimensionless model was to consider the regenerator wall temperature to be constant and having a linear profile between T_H and T_C. With this assumption equation (8) was not required. The other equations were made dimensionless using the dimensionless variables presented in Table 1, where all quantities are properly explained. Substituting the dimensionless variables in the governing equations yields a set of parameters that completely describes the refrigerator. Those parameters are presented in Table 2 with a proper description of their physical meaning.

In dimensionless form the governing equations become,

$$\frac{1}{\Pi_1 - 1}\left[\Pi_{14}\dot{M}_i + \frac{1}{\Pi_{13}}\frac{d(M_i\theta_i)}{dt^*}\right] = \\ = -P_i\frac{d\forall_i}{dt^*} + \frac{\Pi_1}{\Pi_1 - 1}\dot{M}_i\left[\Pi_{14} + \frac{1}{\Pi_{13}}\theta\right] \quad (16)$$

Table 1 Dimensionless variables for the Stirling refrigerator

Time (f is the exciting frequency)	t^*	$t.f$
Axial position in regenerator (L_x is the regenerator length)	x^*	x/L_x
Gas temperature in cold chamber (T_0 is the reference temperature)	θ_1	$\frac{T_1-T_C}{T_H-T_C}\frac{T_C}{T_0}$
Gas temperature in hot chamber	θ_2	$\frac{T_2-T_C}{T_H-T_C}\frac{T_C}{T_0}$
Gas pressure in cold chambe (p_0 is the reference pressure)	P_1	p_1/p_0
Gas pressure in hot chamber	P_2	p_2/p_0
Mass of gas in cold chamber (R_g is the gas constant)	M_1	$\frac{m_1R_gT_0}{p_0V_0}$
Mass of gas in hot chamber (V_0 is the reference volume)	M_2	$\frac{m_2R_gT_0}{p_0V_0}$
Gas volume in cold chamber	$\forall_1$	V_1/V_0
Gas volume in hot chamber	$\forall_2$	V_2/V_0
Piston position (A is the displacer surface)	X_p	x_pA/V_0
Displacer position	X_d	x_dA/V_0
Electrical current in motor (U_P is the motor electrical tension)	I	iR/U_P
Velocity distribution in regenerator	u^*	u/L_xf
Density distribution in regenerator	ρ^*	$\rho R_gT_0/p_0$
Pressure distribution in regenerator	P	p/p_0
Temperature distribution in regenerator	θ	T/T_0

$$P_i\forall_i = M_i(\Pi_{14}+\theta_i/\Pi_{13}) \quad (17)$$

$$\forall_1 = \overline{\forall}_1 - X_d \quad , \quad \forall_2 = \overline{\forall}_2 - (1-\phi^2)(X_d - X_p) \quad (18)$$

$$\partial\rho^*/\partial t^* + \partial(\rho^* u^*)/\partial t^* = 0 \quad (19)$$

$$\Pi_{10}\rho^*\frac{\partial u^*}{\partial t^*} + \Pi_{10}\rho^* u^*\frac{\partial u^*}{\partial x^*} = -\frac{\partial P}{\partial x^*} - \Pi_{11}u^* \quad (20)$$

$$\frac{1}{\Pi_1 - 1}\frac{\partial[\rho^*(\Pi_{14}+\theta/\Pi_{13})]}{\partial t^*} = -\frac{\Pi_1}{\Pi_1-1}\frac{\partial}{\partial x^*}\left[\frac{\partial M}{\partial t^*}(\Pi_{14}+\theta/\Pi_{13})\right] + \Pi_{12}[\theta_r - (\Pi_{14}+\theta/\Pi_{13})] \quad (21)$$

Table 2 Dimensionless parameters for the Stirling refrigerator

$\Pi_1 = \gamma$	→ Ratio between gas specific heats
$\Pi_2 = k_p/(m_pf^2)$	→ Ratio between piston natural frequency (contribution of the spring) and exciting frequency
$\Pi_3 = \frac{U_P\alpha}{R}\frac{A}{m_pV_0f^2}$	→ Ratio between magnetic force and piston inertial forces
$\Pi_4 = \frac{p_0A^2}{m_pV_0f^2}$	→ Ratio between pressure force and piston inertial forces
$\Pi_5 = \frac{k_d}{m_df^2}$	→ Ratio between the displacer natural frequency and exciting frequency
$\Pi_6 = m_p/m_d$	→ Ratio between piston and displacer mass
$\Pi_7 = 1-\phi^2$	→ Proportional factor between rod and piston cross-section area
$\Pi_8 = Lf/R$	→ Ratio between accumulated tension in the inductor and tension across the electrical resistance
$\Pi_9 = \frac{V_0}{A}\frac{\alpha f}{U_P}$	→ Ratio between power transmitted to piston and electrical power source
$\Pi_{10} = \frac{L_x^2f^2}{R_gT_0}$	→ Ratio between kinetic and thermal energy of gas in regenerator
$\Pi_{11} = \frac{12\mu L_x^2f}{p_0a^2}$	→ Ratio between viscous and pressure forces for the gas in the regenerator
$\Pi_{12} = \frac{hL_TT_0}{A_{pass}p_0f}$	→ Ratio between convection to regenerator walls and advection by the fluid in regenerator
$\Pi_{13} = \frac{T_C}{T_H-T_C}$	→ COP of Carnot cycle
$\Pi_{14} = T_C/T_0$	→ Ratio between cold chamber temperature and reference temperature

$$sen(2\pi t^*) = I + \Pi_8\dot{I} + \Pi_9\dot{X}_p \quad (22)$$

$$\Pi_2X_p + \ddot{X}_p = \Pi_3I + \Pi_4\Pi_7(1-P_2) \quad (23)$$

$$\Pi_5X_d + \ddot{X}_d = \Pi_4\Pi_6\Pi_7P_2 + \Pi_4\Pi_6(\phi^2 - P_1) \quad (24)$$

RESULTS AND DISCUSSIONS

The general features of the refrigerator used in the present work as the base case are presented in Table 3. Helium is the working fluid and for the temperatures and pressures encountered here, helium can be assumed an ideal gas with R_g = 2077 J/kg/K.

Table 3 Features of the Stirling Refrigerator employed as base case in the present work

Temperature at the cold heat exchanger: -10 °C
Temperature at the hot heat exchanger: 55 °C
Electric power: 600 W
Cooling capacity: 970 W
COP_{real} (including electric motor): 1.6
Phase angle: 73.2°
Frequency (Hz): 60
Piston amplitude: 22.4 mm
Displacer amplitude: 26.8 mm

The corresponding values of the dimensionless parameters for the refrigerator employed as the base case are presented in Table 4.

Table 4 Values of the dimensionless parameters for the refrigerator employed as the base case

Π_1=1.7	Π_2=0	Π_3=33.1	Π_4=24.3
Π_5=37.6	Π_6=4.4	Π_7=0.6	Π_8=3.9
Π_9=1.5	Π_{10}=6.0x10^{-6}	Π_{11}=1.4x10^{-3}	Π_{12}=128.6

A first aspect to be explored is the sensitiveness of the refrigerator performance to each of the dimensionless parameters. In this regard Table 5 was prepared.

Table 5 Sensitivity of the refrigeration performance to 10 % variation in each dimensionless parameter

	$\dot{Q}_C(W)$	$\dot{W}_{elet}(W)$	COP_{real}
Π_{11}	68.4%	62.1%	5.9%
Π_5	21.2	29.9	-8.6
Π_1	-19.8	-11.5	-8.4
Π_9	-18.7	-21.2	2.5
Π_4	-16.8	-17.7	0.8
Π_8	-13.2	-14.6	1.3
Π_7	7.2	4.4	2,8
Π_{12}	3.4	3.5	-0.1
Π_{10}	1.7	1.7	-0.1
Π_6	1.3	1.7	-0.4
Π_3	0.5	0.2	0.3
Π_2	-0.2	-0.3	0.0

The results in Table 5 present the percentage variation in the cooling capacity, electric power consumption, and refrigerator COP_{real} for a variation of 10% in each of the twelve dimensionless parameters indicated. For COP_{real} the cooling capacity is divided by the electric power consumption, in contrast to COP_{termo} where the thermodynamic power deliver to the gas is employed. The parameters Π_i in Table 5 are listed from the most to the least influential in the cooling capacity. Variations in the performance quantities for each dimensionless parameter Π_i were obtained from the sensitivity coefficient $\partial/\partial\Pi_i$ which was calculated by varying the corresponding dimensionless parameter by 1% from its original value while all others parameters were kept constant. The performance quantity was then obtained for the two values of the dimensionless parameter and the derivative $\partial/\partial\Pi_i$ was calculated numerically. Once $\partial/\partial\Pi_i$ was obtained, variations of $\dot{Q}_C$, $\dot{W}_e$ and COP_{real} were calculated from

$$\Delta(\,) = [\partial(\,)/\partial\Pi_i]\,\Delta\Pi_i. \qquad (25)$$

According to Table 5 the most influential parameter in the cooling capacity is Π_{11} which is the ratio between viscous and pressure forces inside the regenerator. That result reflects the importance of the regenerator in the refrigerator performance. A ten percentage increase in Π_{11} results in a 68.4% increase in the refrigerator cooling capacity. Because the regenerator channel height a appears in the denominator of Π_{11} raised to the square power, a 5% decrease in a increases the cooling capacity by almost 70%. In this case, for all other dimensionless parameters to be kept constant, because of the increase in the viscous forces the electric power delivered to the refrigerator has to be increased by approximately 62%, as seen from Table 5.

The others most influential dimensionless parameters regarding the refrigerator cooling capacity are Π_5, Π_1, Π_9 and Π_4. Parameter Π_5 represents the ratio between the displacer natural frequency and the exciting frequency and its influence in the cooling capacity indicates the high sensitivity of both mass and spring stiffness in the refrigerator performance. Parameter Π_1, is only affected by the working fluid and is more difficult to be changed. Parameter Π_9 is related to the electric efficiency of the motor and can be decreased by increasing the amount of electric power that is converted into mechanical power transmitted to the piston. The fifth most influential parameter in the cooling capacity of the refrigerator is Π_4 and as its value decreases the cooling capacity increases. This parameter reflects the ratio between the pressure forces that move the working gas from one chamber to the other and the piston inertial force. Because of the oscillatory motion of the piston, the inertial force affects positively the refrigerator cooling capacity. The dimensionless parameters Π_8 and Π_7 have a moderate to low influence on the cooling capacity, and Π_{12}, Π_{10}, Π_6, Π_3, and Π_2 have small influence on both the cooling capacity and the electric power consumption.

According to Table 5, the COP_{real} is less affected by the dimensionless parameters than the cooling capacity and the electric power. Only Π_5, Π_1 and Π_{11} have a moderate to low influence on the refrigerator overall performance coefficient. The influence of the other dimensionless parameters on the performance coefficient is much less significant.

Use of the dimensionless parameters is a convenient manner to explore different families of Stirling refrigerators. In what follows some of these families will be presented.

Different refrigerators having the same features of the base case shown in Table 3, except for the cooling capacity and the electric power consumption, are shown in Table 6. In the lower part of the table, schematic views of the corresponding refrigerators are presented in scale for comparisons.

Table 6 Influence of gas volume on the refrigerator cooling capacity for the base case of Table 3

	$\beta_V = 1.2$	$\beta_V = 1$	$\beta_V = 0.8$	$\beta_V = 0.5$
$\dot{W}_e(W)$	716	600	484	309
$\dot{Q}_C(W)$	1150	969	793	497

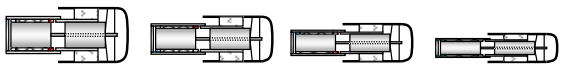

The parameter that was varied for the refrigerators indicated in Table 6 is the gas volume. Four refrigerators are depicted: the base case ($\beta_V = 1$), a refrigerator having 20% more volume than the base case ($\beta_V = 1.2$), 80% less volume ($\beta_V = 0.8$), and half of the volume of the base case ($\beta_V = 0.5$). All refrigerators

in Table 6 have the same operating temperatures for the hot and cold chambers, the same COP_{real}, the same operating phase angle, mean pressure, frequency, and piston and displacer amplitudes. As seen from the table, both the cooling capacity and the electric power consumption are directly proportional to β_V.

Family of refrigerators having the same volume of gas, same operating temperatures for the hot and cold chambers, same COP_{real}, same cooling capacity and electric power consumption, same phase angle and operating frequency, are presented in Table 7 for different piston and displacer area. The area multiplying factors vary from 0.5 to 1.2. Because the gas volume was kept constant, the piston and displacer moving amplitudes varied accordingly.

Table 7 Influence of piston and displacer area on the base case refrigerator of Table 3

	$\beta_A = 1.2$	$\beta_A = 1$	$\beta_A = 0.8$	$\beta_A = 0.5$
$x_{p,max} - x_{p,min}\,(mm)$	18.7	22.4	28.0	45.0
$x_{d,max} - x_{d,min}\,(mm)$	22.3	26.8	33.4	53.6

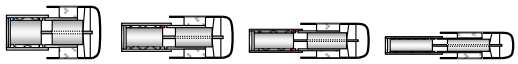

The parameter that was varied for the refrigerators indicated in Table 8 is the gas average pressure. Again, all other quantities were kept constant including the volume occupied by the refrigerating gas. The average pressure multiplying factors vary from 0.5 to 1.2.

Table 8 Influence of gas average pressure on the base case refrigerator of Table 3

	$\beta_P = 1.2$	$\beta_P = 1$	$\beta_P = 0.8$	$\beta_P = 0.5$
$\dot{W}_e(W)$	718	600	484	308
$\dot{Q}_C(W)$	1143	969	788	503

As indicated in Table 8, both the cooling capacity and the electric power consumption are directly proportional to β_P.

The last family of refrigerators explored here are those presented in Table 9, where the varying parameter is the operating frequency. Similar to the gas volume and the gas average pressure, both the cooling capacity and the electric power consumption are also directly proportional to β_F, as indicated in the table. Again, it should be stressed, that except for the operating frequency all other parameters including the gas volume and the gas operating pressure are kept constant.

The previous discussion focused on the dimensionless parameters related to the refrigerator designing characteristics expressed by Π_1 to Π_{12}. Now attention will be turned to the dimensionless parameters related to the reservoir operating temperatures T_H and T_C that is Π_{13} and Π_{14}, as indicated in Table 2.

Table 9 Influence of operating frequency on the base case refrigerator of Table 3

	$\beta_F = 1.2$	$\beta_F = 1$	$\beta_F = 0.8$	$\beta_F = 0.5$
$\dot{W}_e(W)$	722	600	480	299
$\dot{Q}_C(W)$	1183	969	773	475

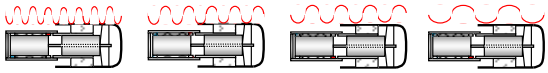

In what follows the interest is to explore how COP_{real} varies with Π_{13} and Π_{14} while Π_1 to Π_{12} are kept constant. Simulations for $COP_{real} = COP_{real}(\Pi_{13}, \Pi_{14})$ indicated that for Π_{13} varying from 3 to 30 and for Π_{14} varying from 0.6 to 1.0, which encompass variations of T_C of more than 100 degrees, COP_{real} is virtually independent of Π_{14} and can be expressed as,

$$COP_{real} = 4.7 - 13.5 / \Pi_{13} = 4.7 - 13.5 / COP_{Carnot} \qquad (26)$$

From equation (26) it is seen that the maximum value for COP_{real} achieved by the Stirling refrigerator investigated here and represented by the dimensionless parameters indicated in Table 4 is 4.7. Figure 3 illustrates the dependence of COP_{real} with Π_{13} as indicated in equation (26). Also shown in the figure is COP_{Carnot} for comparisons.

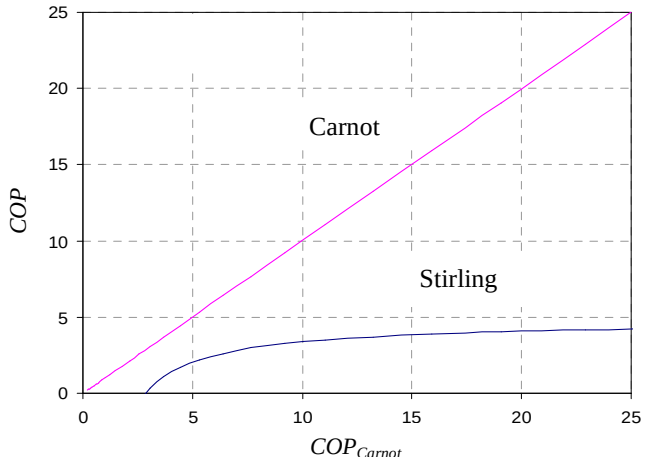

Figure 3 Variation of COP with Π_{13} for the Stirling refrigerator

According to Figure 3, there is a minimum value for $\Pi_{13}=COP_{Carnot}$ in which COP_{real} is positive, that is *2.9*. Therefore, for the Stirling refrigerator to generate cooling capacity, T_H/T_C has to be smaller than *1.34*.

The efficiency of the Stirling refrigerator can be defined as,

$$\eta = COP_{real}/COP_{Carnot} = COP_{real}/\Pi_{13} \quad (27)$$

and, making use of equation (26), η can be written as,

$$\eta = 4.7 / \Pi_{13} - 13.5 / \Pi_{13}^2 \quad (28)$$

From equation (28) the maximum efficiency of the present Stirling refrigerator can be determined. Its value is 42% and occurs for $\Pi_{13}=5.7$.

A last question to be addressed is related to the feasibility of using Stirling refrigerators as alternative for other technologies. In this regard, it is useful to recall that in the present investigation the temperature of the fluid exiting the hot and cold heat exchangers was taken as the corresponding temperature of the hot and cold reservoir, respectively. Thus, existing thermal resistances between the working fluid and the ambient to be cooled as well as the hot ambient should be included in dealing with more real situations. Because of those resistances, a useful approach is to consider additional temperature differences by reducing T_C and increasing T_H. Typical values are $10\ ^oC$ for the cold ambient and $15\ ^oC$ for the hot ambient.

Comparing some selected applications with the present Stirling refrigerator operating at its highest efficient, it was observed that the Stirling refrigerator can be a competitive alternative in applications such as vending machines, automotive applications (small refrigeration compartment for liquid cooling), domestic refrigeration and some electronics applications. The Stirling refrigerator is not competitive for medical applications, freezers and air-conditioning.

CONCLUSION

A free piston Stirling refrigerator was analysed in terms of a set of basic differential equations that described the behaviour of the working gas as well as the dynamics of the moving parts. The refrigerator design features and its performance were investigated through fourteen dimensionless parameters. The model was comprehensive enough to explore different aspects of the machine. Regarding the refrigerator cooling capacity it was observed that the regenerator plays a very important role, together with the proper design of the piston and displacer oscillating mechanism. The performance coefficient included the effect of the mechanical and electrical parts in the calculation of the thermodynamic power delivered to the working gas. It was shown that the maximum coefficient of performance achieved with the present configuration was 42% of that the Carnot cycle.

The present analysis can be easily extended to other types of Stirling machines and can be used as a valuable guide in design for applications and in comparisons with other technologies.

REFERENCES

[1] Walker G., Reader G., Fauvel O. and Bringham E. R., *The Stirling Alternative*, Gordon and Breach Science Publishers Yverdon, Switzerland, 1994.

[2] Berchowitz D. M., McEntee J. and Welty, S., Design and Testing of a 40W Free-Piston Stirling Cycle Cooling Unit, *Proceedings of the 20th International Congress of Refrigeration*, Sydney, Australia, 1999.

[3] Organ A. J., *Thermodynamics and Gas Dynamics of the Stirling Cycle Machine*, Cambridge University Press, 1992.

[4] Urieli I. and Berchowitz D. H., *Stirling Cycle Engine Analysis*, Adam Hilger Ltda., 1984.

[5] Huang B. J., and Lu C. W., Split-type Free-displacer Stirling Refrigerator Design Using Linear Network Analysis, *Cryogenics*, Vol. 36, 1996, pp. 1005-1017.

[6] Huang B. J, and Chen H. Y., Modeling of Integral-type Stirling Refrigerator Using System Dynamics Approach, *International Journal of Refrigeration*, Vol. 23, 2000, pp. 632-641.

[7] Kaushik S. C. and Kumar S., Finite Time Thermodynamic Evaluation of Irreversible Ericsson and Stirling Heat Engines, *Energy Conversion & Management*, Vol. 42, 2001, pp. 295-312.

[8] Ataer O. E., Numerical Analysis of Regenerators of Free Piston Type Stirling Engines Using Lagrangian Formulation, *International Journal of Refrigeration*, Vol. 25, 2002, pp. 640-652.

[9] McFarlane P., Semperlotti F. and Sen M., Mathematical Model of an Air-Filled Alpha Stirling Refrigerator, *Journal of Applied Physics*, Vol. 114, 2013, 144508.

[10] Heidrich J., Prata A.T. and Lilie D.E.B, Heat and Fluid Flow in a Free Piston Stirling Refrigerator, *Proceedings of the International Conference on Compressor and their Systems*, pp. 81-90, London, September 4-7, 2005.

[11] Patankar S. V., *Numerical Heat Transfer and Fluid Flow*, McGraw-Hill Book Company, 1980.

HEFAT2015
11th International Conference on Heat Transfer, Fluid Mechanics and Thermodynamics
20 – 23 July 2015
South Afrika

A NEW APPROACH FOR EFFICIENT DEHUMIDIFICATION

Bronchart F.*, De Paepe, M., Demeyer, P. and Van linden, V.
*Author for correspondence
Institute for Agriculture and Fisheries Research,
Merelbeke, 9820
Belgium
Department of Flow, Heat and Combustion Mechanics
Ghent University
Gent,9000
Belgium
E-mail: filip.bronchart@ilvo.vlaanderen.be

ABSTRACT

Dehumidification of air is an important economic activity responsible for high primary energy use. Several technologies are available that lower both, cost and primary energy use, such as heat pump dehumidification systems, desiccant dehumidification wheels, or other absorption systems. However, the drying efficiency of these technologies is still far below the expected efficiency as prospected by thermodynamic analyses based on the second law. This paper looks into the thermodynamics of drying and proposes a novel dehumidification technology. The proposed system consists of a heat mass exchanger and a mechanical vapour compression unit and is called a vapour heat pump. First, humid air is brought in contact with a hygroscopic salt solution in the exchanger unit and second, the diluted salt solution is reconcentrated by the mechanical vapour compression unit. An analysis of the vapour heat pump indicates a dehumidification efficiency of 6.6 to 9.3. A successful development of the vapour heat pump can have an important effect on the worldwide energy use and sustainability.

INTRODUCTION

Water vapour is a component of air. The mass fraction of water vapor in air at room temperature (20°C) is around 1.5%. Despite this small mass fraction of water vapour in air, it has a large impact on the air properties. Two major processes take place: water vapour can be removed through condensation or added by evaporation. In either case, water undergoes a phase transition, which influences the air temperature. Based on these principles, the energy and/or enthalpy of air is determined by its temperature (sensible heat) and by its vapour content (latent heat).

We need an appropriate vapour content in process air for the different human activities, This could be realized by humidifying or dehumidifying the air. Humidification means adding vapour to the air. As a consequence, the latent heat of the air is also increased. In the case of adiabatic humidification, an increase in latent heat is compensated by a reduction in sensible heat (1st law). Dehumidification means reducing the vapour in the air, and it is the opposite of humidification. However, there is an important thermodynamic difference between both: humidification is a spontaneous process that occurs when liquid water is making contact with unsaturated air. In contrast, dehumidification is not a spontaneous process. Dehumidification is thus more complex process.

Dehumidified air can be used in a wide range of applications like industrial drying or air conditioning. According to [1], drying in the industry is responsible for as much as 15% of its total energy use. [2] mentions that this share for drying increases up to 25% of the total energy required in the developed countries. Dehumidified air for air conditioning is not only important for buildings but also for greenhouses. In Belgium and the Netherlands, for example, dehumidification in greenhouses is responsible for 25% of its energy demand [3]. Greenhouses consume up to 64% of the total energy demand of the agricultural sector in Flanders [4].

The economic importance of dehumidification and the environmental concerns about primary energy saving necessitate the development of efficient drying or dehumidification technologies. Drying or dehumidification, after all, has a high energy demand. Dryer energy efficiency, which is the ratio of the latent heat of evaporated water to the total heat input, typically ranges from 20 to 60% [5]. Much higher efficiencies are theoretically possible because for drying a high quality energy (fossil fuel, electricity) is used to a obtain a low quality result (dehumidified air or a dried product). To that respect, [6] calculated that the maximal theoretical performance for dehumidification of air with 85%RH is 112 (J dehumidification per J exergy input).

In industry, a higher drying performance is achieved when using a superheated steam dryer [7]. In such a system, the product to dry are put in contact with superheated steam. The product adsorbs heat and evaporates. As a consequence, the steam is becoming almost saturated and has a lower drying capacity. To regenerate, a part of the more saturated steam is compressed and then condenses at a higher temperature. This heat of condensation is delivered back to the steam, resulting in the desired strong drying superheated steam. Net energy use in superheated steam dryers is as low as 0.7-1 MJ per kg of evaporated water, which results in a drying efficiency of 2.5 to 3.5.

Despite the economic success of superheated steam dryers, they cannot be widely applied to all products due to the high drying temperatures. Therefore, convective drying techniques are still being used for a lot of products. At present, 85% of the industrial dryers are convective air dryers [5]. Traditionally, such convective air dryers heat air by burning primary energy and vent the humidified air. More efficient air dehumidification techniques are drying heat pumps [2], desiccant drying systems, infra-red drying or a combination of these (hybrid system) [8]. Nevertheless, market penetration of these more efficient convective air dry systems is rather small (Mujumdar, 2007a).

[8,9] state that an intelligent combination of dryer types is critical for achieving a higher performance . They say that this "intelligent combination" depends on the "creativity" of the researcher. It seems that until now, the creativity of the researchers for developing dryers that operate at moderate temperature is minimal, if you compare the potential of highly efficient dehumidification and the lack of an appropriate technology. In this paper, we propose such an appropriate dehumidification technique, based on the analysis of the irreversibility in a dehumidification process. The efficiency of this dehumidification technique is modelled and presented.

NOMENCLATURE

A	[m²]	Surface
cp	[J/kg/K]	Specific heat
D	[J]	Dehumidification
eqRH	[%]	Equilibrium relative humidity of hygroscopic salt solution
E	[J]	Energy
EX	[J]	Exergy or availability
EXD	[J]	Exergy destruction or loss of exergy
l_{23}	[J/kg]	Heat of phase change of water from liquid to vapour
m	[kg]	Mass of water
n	[mol]	Mols of water
p	[Pa]	pressure
Q	[J]	Heat
r	[s/m]	Transfer resistance
R	[J/mol/K]	Ideal gas constant
RH	[%]	Relative humidity
T	[K]	Temperature
V	[m³]	Volume

Special characters

η	[%]	Efficiency
ρ	[kg/m³]	Density
Δ	[-]	Difference between

Subscripts

a	air
A	condition A
B	condition B
c	condensing
COL	cold surface
COND	the condensation water
cool	cooling
deh	dehumidification
e	environment
FF	falling film
HEX	heat exchanger
HMEX	heat mass exchanger
ht	heat transfer
H2O	water
hum	humidification
i	species i
inp	input
mt	mass transfer
MVC	mechanical vapour compression
out	output
SOR	sorbent
VENT	ventilation
VHP	vapour heat pump

THE EFFICIENCY OF DEHUMIDIFICATION

Dehumidification reduces the water vapour fraction in the air and its latent heat (~2.5 MJ/kg). For adiabatic dehumidification this reduction of latent heat is compensated by a gain in sensible heat, resulting in a constant enthalpy of the system.

The efficiency for dehumidification is

$$\eta_{deh} = \frac{D}{E_{inp}}$$

The energy input can be primary energy or electricity, which is the generic driving force for thermodynamic cycles.

For electricity holds (see [10]):

$$E_{inp} = EX_{inp}$$

and

$$EX_{inp} = EXD + EX_{out}$$

So, the efficiency of dehumidification can be expressed as

$$\boldsymbol{\eta_{deh}} = \frac{\boldsymbol{D}}{\boldsymbol{EXD + EX_{out}}} \quad (1)$$

Equation (1) indicates that the efficiency of dehumidification is inversely correlated to the exergy destruction in its processes and the exergy content of its output

(dehumidified air). The output is a setting of the dehumidification device and is not variable. The efficiency of dehumidification can thus only be optimized by minimizing the exergy destruction in its processes.

Let us have a look at the thermodynamics and the different exergy destructions in the processes of dehumidification.

Based on the second law of thermodynamics, the exergy destruction during (spontaneous) humidification or the minimal external exergy input for dehumidification is [6]

$$\boldsymbol{EXD_{hum}} = \Delta \boldsymbol{EX_{deh}} \approx -\boldsymbol{n_{H2O}}.\boldsymbol{R}.\boldsymbol{T_e}.\ln(\boldsymbol{RH}) \approx -\boldsymbol{m_{H2O}}.\boldsymbol{T_e}.\boldsymbol{l_{23}}.\left(\frac{1}{T_a}-\frac{1}{T_c}\right) \quad (2)$$

This equation takes only the mass transfer process between vapour and liquid water into account. In this process, the heat resulting from a phase change, is transferred to the liquid or solid material. Possible heat transfer processes that simultaneously occur due to difference in temperature between the liquid or solid material and the air are not considered.

From Equation (2), we conclude that

- Dehumidification needs only a small exergy input (20kJ/kg water at 85%RH, 90kJ/kg water at 50%RH). This illustrates the high potential for efficient dehumidification.
- The minimal exergy input for dehumidification depends on the drying depth (RH). Strong drying requires a logarithmically higher input.

The external driving force for dehumidification is provided by (see Figure 1)

- Cooling: The humid air is exposed to a cold surface at a temperature below its condensing temperature, and the vapour in the air condenses on that surface.
- Sorption: A liquid or fixed sorbent that has the capacity to adsorb vapour of unsaturated air is put in contact with the air. depends on The drying state of the sorbent is determinant for its affinity to adsorb vapour.

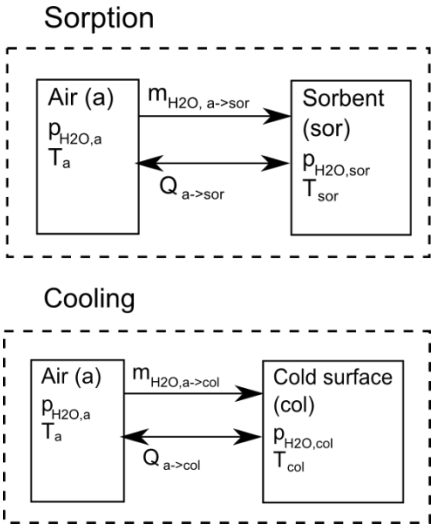

Figure 1 Schematic representation of dehumidification through sorption and cooling. There is a mass flow at a higher to a lower pressure. The heat flow depends on the temperatures. The regeneration of the sorbent and the cold surface are not illustrated.

For dehumidification by cooling, the following processes take place

1. Cooling of the air until its condensing temperature (T_c) is reached.
2. Further cooling of the air under its condensing temperature.
3. Simultaneous mass transfer of water vapour to liquid (condensation).

The equation for the loss of exergy during dehumidification by cooling, is (see [6,10])

$$\boldsymbol{EXD_{deh,cool}} = -\int \boldsymbol{n_{H2O,a\to col}}\,\boldsymbol{R}\,\boldsymbol{T_e}\ln\left(\frac{\boldsymbol{p_{H2O,col}}}{\boldsymbol{p_{H2O,a}}}\right) - \int \boldsymbol{Q_{a\to col}}\,\boldsymbol{T_e}\left(\frac{1}{T_a}-\frac{1}{T_{col}}\right) \quad (3)$$

For dehumidification by sorption, the following processes take place:

1. Mass transfer of water vapour at a higher pressure $p_{H2O,a}$ to the sorbent at a lower pressure $p_{H2O,sor}$. The sorbent is absorbing the energy of the phase change.
2. Depending on the temperature of the sorbent, also heat exchange ($Q_{a,sor}$) can take place to some extent.

The equation for the loss of exergy during dehumidification by sorption, is

$$\boldsymbol{EXD_{deh,sor}} = -\int \boldsymbol{n_{H2O,a\to sor}}\,\boldsymbol{R}\,\boldsymbol{T_e}\ln\left(\frac{\boldsymbol{p_{H2O,sor}}}{\boldsymbol{p_{H2O,a}}}\right) - \int \boldsymbol{Q_{a\to sor}}\,\boldsymbol{T_e}\left(\frac{1}{T_a}-\frac{1}{T_{sor}}\right) \quad (4)$$

The first term in both equations describes the dehumidification, while the second term describes the heat transfer.

Some characteristics of the different systems are here listed:

- For dehumidification by cooling, the heat transfer term is high. In contrast, this term is minimal during sorption or can be zero in case the temperatures of the sorbent and the air are equal.
- The proportion in exergy destruction by heat transfer compared to mass transfer for dehumidification by cooling depends on the conditions. Exergy destruction due to heat transfer will become more important when the air is dryer and at a lower temperature.
- For “adiabatic dehumidification” (for a description, see above), the dehumidified air needs to be heated. For “sorption dehumidification”, only the heat of phase change needs to be transferred to the air. However, for “cooling dehumidification”, also the sensible heat of the cooling needs to be retransferred to the air, resulting in an additional exergy destruction.

We conclude that dehumidification by sorption is more attractive because it results in a lower quantity of heat transfer and thus a lower exergy destruction.

The exergy loss (EXD) is not only proportional to the number of processes involved (quantity), it is also proportional to a quality difference ($\ln(p_1/p_2)$ or $(1/T_1\text{-}1/T_2)$). The smaller that difference, the less exergy is lost.

This quality difference is related to the driving force of the process, as described by the following equations:

$$Q_{B\to A} = \frac{\rho\ cp\ A}{r_{ht}}(T_B - T_A) \quad (5)$$

$$\boldsymbol{m_{i,B\to A} = \frac{A}{r_{mt}}\ (\rho_{i,B} - \rho_{i,A})} \quad (6)$$

Based on the equations 3 to 6, a sufficient process speed with a minimal exergy destruction can be realized through a minimal resistance factor for mass (r_m) and heat (r_h) transfer in combination with a maximal surface (A). Indeed, this will result in minimal temperature differences or vapour pressure differences.

Another factor that determines the exergy efficiency of the dehumidification device is its pressure drop:

$$\boldsymbol{EXD = -V * \Delta p} \quad (7)$$

Integration of equation 7, combined with the ideal gas law, yields the equation for exergy destruction through mass transfer ($n\ R\ T\ \ln(p_1/p_2)$). Those similarities are there because both processes have the same driving force.

In the next section, we propose an efficient dehumidification device starting from these analyses. The device is called a "vapour heat pump", because it upgrades the energy in vapour to energy in sensible heat. The name is chosen based on the analogy with a classic heat pump that upgrades sensible heat at a lower temperature into sensible heat at a higher temperature.

THE DESIGN OF AN EFFICIENT DEHUMIDIFICATION DEVICE: THE VAPOUR HEAT PUMP

The design of the vapour heat pump is based on the principles described in the previous section. It consists of (

A **dehumidification device as described above, is currently being developed in our lab. An appropriate matrix material has been chosen [18] for the HMEX. A pilot for the MVC of the hygroscopic salt solution is under construction.**

The next section is presenting the modelling of the vapour heat pump's dehumidification efficiency.

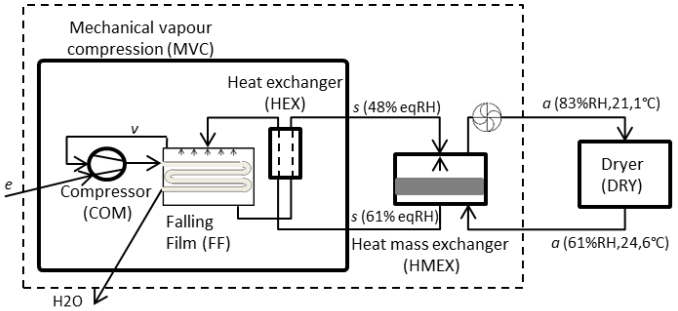

Figure 2)

- a counter flow heat mass exchanger (HMEX) between the air and the liquid desiccant solution (such as a $CaCl_2$ or LiCl solution), and,
- a mechanical vapour compression (MVC) unit to reconcentrate the diluted salt solution.

Here are some more details on the vapour heat pump:

- The counter flow HMEX consist of
  - a distribution unit of concentrated desiccant solution on the top
  - a matrix material through which the salt solution flows by gravity
  - a drain unit for the diluted hygroscopic salt solution
  - an air inlet at the bottom and an air outlet at the top
- Humid air is entering the HMEX at the bottom and is flowing through the matrix. The matrix surface is covered with a thin layer (~0.05mm) of a hygroscopic salt solution that flows down by gravity and has intensive contact with the upward flowing air (counter flow).
- For an efficient counter flow design of the HMEX, the hygroscopic capacity of the air stream and salt solution stream must be similar. The hygroscopic capacity of a stream (kg/s) is defined as the mass of absorbed water, per unity change of the (equilibrium) relative humidity and per mass of substance multiplied with its flow rate. For such a similar hygroscopic capacity, the mass ratio between the salt solution and the air flow is small and the HMEX is called "low flow" ([11,12,13,14]).
- Part of the vapour in the air is absorbed by the hygroscopic salt solution. During that process, the latent heat of evaporation (~2.5 MJ/kg) and the differential enthalpy of dilution (~50-300kJ/kg, see [15]) are transformed into sensible heat, which is absorbed by the salt solution. Most of this sensible heat, however, is transferred to the air (approximating adiabatic dehumidification) because of the low thermal capacity of the salt solution flow compared to the air flow.
- The dried and heated air is then transferred to the drying unit, and the diluted salt solution to the MVC unit.
- The general principle of MVC is as follows: A liquid is boiling in contact with a surface. The produced vapour is compressed. This compressed vapour is then brought in

contact with the opposite side of the surface ("thermal contact"). The vapour is condensing and transferring the heat of that phase change to the surface, a process that allows the liquid at the other side to continue boiling.

- Several design possibilities exist for MVC-units, for example bundle boiling, flow boiling in evaporation tubes, and vertical or horizontal falling films (see [16,17]). An optimal efficiency of the vapour heat pump will depend on an optimal design of the MVC-unit.
- A heat exchanger is exchanging the heat between the incoming and the outgoing salt solution (
-
-

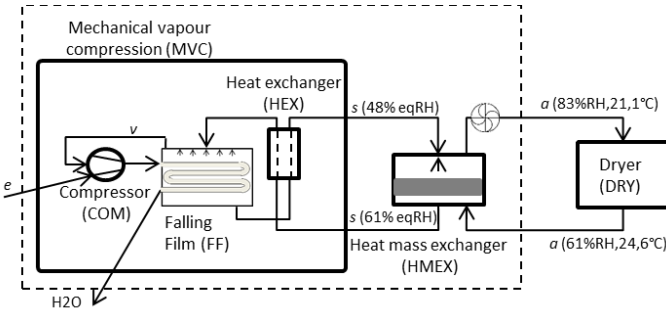

-

Figure 2).

- In such a vapour heat pump, the hygroscopic salt solution is the "refrigerant" of this open system.
- An additional advantage of the proposed system is that it can perform well in a corrosive environment such as for wood drying. The coils of the evaporator of a drying heat pump will typically have corrosion problems.

A dehumidification device as described above, is currently being developed in our lab. An appropriate matrix material has been chosen [18] for the HMEX. A pilot for the MVC of the hygroscopic salt solution is under construction.

The next section is presenting the modelling of the vapour heat pump's dehumidification efficiency.

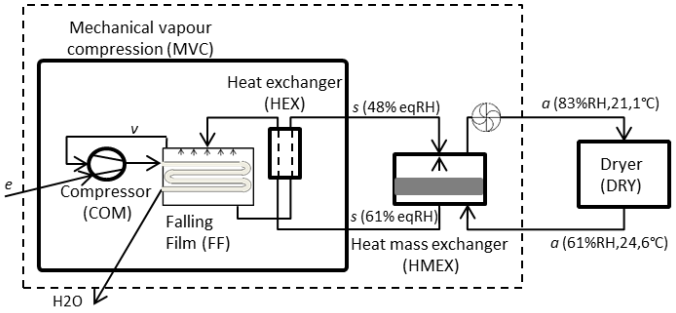

Figure 2 Representation of the basic principles of a vapour heat pump. The indicated values for air and salt solution are typical values for greenhouse dehumidification and vary depending on the application. The dashed line is the boundary for the exergy analysis of the dehumidification device. *a* stands for air, *e* for electricity, *H2O* for liquid water, *s* for liquid hygroscopic salt solution and *v* for vapour.

EFFICIENCY ANALYSES OF THE VAPOUR HEAT PUMP

Technical data and calculation method

Six different air conditions are modelled (see Table 1 displays the air characteristics per kg dry air under different drying conditions. The exergy difference between the dried and humid air is higher for lower RHs, (higher quality difference, see Equation 1) and for higher temperatures (higher quantity, see equation 1).

Table 1). The air outlet conditions in Table 1 are given for adiabatic drying conditions (see section **Fout! Verwijzingsbron niet gevonden.**). This is an approximation: adiabatic drying is not a spontaneous process, some additional exergy input is required and will result in somewhat higher output temperatures.

The vapour heat pump is modelled under the following conditions:

- The characteristics of the HMEX are studied in our lab and will be published later. The average driving force for the heat transfer is around 2°C. For the mass transfer, a RH difference of 10-20% is used, depending on the drying rates. The pressure drop is small and approximates 20 Pa. Exergy destruction is calculated according to Equations 3 and 4.
- The heat transfer in a MVC-unit is around 15kW/m² for a 4°C temperature difference.
- The heat exchanger (HEX) between the incoming and outgoing salt solution is supposed to have an average temperature difference of 5°C.
- Isentropic efficiency of the compressor is 70% (see Groll, 2012).
- Axial fans are used. Their exergetic efficiency is 40% based on values of the commercial supplier Ventomatic.
- For calculation equations that are not mentioned, refer to a general thermodynamic handbook (e.g. Moran and Shapiro, 1998).
- Air values are calculated per kg dry air.

Results and discussion

Table 1 displays the air characteristics per kg dry air under different drying conditions. The exergy difference between the dried and humid air is higher for lower RHs, (higher quality difference, see Equation 1) and for higher temperatures (higher quantity, see equation 1).

Table 1: Six different air conditions as used in the analyses of the vapour heat pump. The air outlet conditions are calculated for an adiabatic system. Values are expressed for 1 kg of dry air.

$T_{a,inp}$ (K)	$RH_{a,inp}$	$T_{a,out}$ (K)	$RH_{a,out}$	D (J)	Δm_{H2O} (kg)	ΔEX (J)

1	293	0.9	299	0.5	6166	-0.0025	138
2	293	0.6	299	0.3	5941	-0.0024	276
3	305	0.9	313	0.5	8240	-0.0034	206
4	305	0.6	314	0.3	8479	-0.0035	419
5	325	0.9	336	0.5	11941	-0.0050	378
6	325	0.6	338	0.3	12852	-0.0054	723

Table 2 depicts the corresponding exergy destructions and efficiency of the vapour heat pump for the air conditions.

Table 2: Simulated exergy loss (EXD) of the different components of the vapour heat pump as described in Fig. 2 and its dehumidification efficiency (η_{deh}). The numbering 1 to 6 refers to the air conditions in Table 1. The EXD of the pressure drop in the HMEX and in the ventilator is summed in the group VENT. Σ represent the summation of the exergy destruction of the different processes in the concerning device.

	HMEX	VENT	Σ HMEX	FF	COM	HEX	COND	Σ MVC	Σ VHP	η_{deh}
1	152	41	193	50	100	54	110	314	507	9.6
2	200	41	242	48	145	70	106	369	611	6.7
3	201	41	242	66	135	73	149	424	666	9.5
4	285	41	326	68	209	101	154	532	858	6.6
5	287	41	328	96	200	107	221	624	952	9.0
6	429	41	470	104	323	156	238	820	1291	6.4

From the table, we can conclude that

- The MVC-unit is responsible for the largest part of the exergy destruction.
- In the presented design, the heat of the condense water dissipates to the environment during cooling. This results in exergy losses (column COND in Table 2). For a vapour heat pump, the recuperation of the sensible heat of both fluxes is thus important. However, the possibilities will also depend on the energy balances of the MVC unit (inputs are the diluted salt solution and electricity of the compressor, outputs are the concentrated salt solution and liquid water) which are not integrated in this simulation study.
- The efficiency (η_{deh}) is only slightly influenced by the air temperature. In contrast, the impact of the relative humidity is more pronounced, as expected: stronger drying needs will result in a lower dehumidification efficiency.
- The average calculated efficiency for dehumidification is 9.3 for humid conditions (RH 0.9→0.5) and 6.6 for dry conditions (RH 0.6→0.3).

For comparison, the actual efficiencies of moderate temperature dryers in industry are:

- Conventional air dryers have efficiencies of 0.2 to 0.6 [5].
- Advanced air dryers like heat pump dryers have efficiencies of 1 to 3 [2]; desiccant wheel assisted dryers have efficiencies close to 1 [8].

Compared to those values, the proposed vapour heat pump has the potential to cause a massive improvement in industrial drying efficiency. Furthermore, because drying processes take up as much as 15% of the total energy, used by industry [1], a successful development of the vapour heat pump can significantly reduce the energy use worldwide. A successful economic implementation will depend on the combination of energy savings, minimal costs, and a good reliability.

CONCLUSIONS

Based on second law analyses, efficient dehumidification is feasible. However, even the best available technology still has a low dehumidification efficiency. A comprehensive thermodynamic analysis was performed to explain that discrepancy.

Dehumidification by sorption, in contrast to cooling, is more attractive for an efficient dehumidification device because the processes of sensible cooling and redistributing the heat to the air are avoided. Of course, the regeneration of the sorbent should also be efficient.

This paper presents a novel dehumidification device with a higher efficiency. The device consists of a heat mass exchanger, containing a salt solution that absorbs the water vapour in the humid air during intensive contact with the air. The diluted salt solution is regenerated or reconcentrated in a mechanical vapour compression unit, in which the salt solution boils. The produced vapour is compressed and condenses at a higher temperature, thereby producing heat for the boiling process. Such a system will be called a vapour heat pump.

The performance of the vapour heat pump is modelled by studying and modelling all processes that take place in the heat mass exchanger and in the mechanical vapour compression unit.

The dehumidification efficiency of the vapour heat pump is on average 9.3 for humid air conditions (RH from 0.9 to 0.5) and 6.6 for dry air conditions (RH from 0.6 to 0.3). This means a huge efficiency improvement compared to traditional drying techniques (η_{deh}~0.2-0.6) and advanced drying technologies like heat pump drying (η_{deh}~1-3) and desiccant wheel dryers (η_{deh}~1).

A successful development of the vapour heat pump can have a considerable impact on the global energy use and the overall sustainability due to the large share of drying in the global energy consumption.

REFERENCES

[1] Kemp, I. C., Reducing dryer energy use by process integration and pinch analysis, Drying Technology, pp. 2089-2104, 2005

[2] Minea, V., Industrial Drying Heat Pumps, 2011, pp. 1-70

[3] Campen, J. B., Bot, G. P. A., and de Zwart, H. F., Dehumidification of greenhouses at northern latitudes, Biosystems Engineering, pp. 487-493, 2003

[4] Bergen, P., Vander Vannet B., and Overloop S., MIRA 2009. Deelsector glastuinbouw., 2010,

[5] Mujumdar, A. S., Handbook of Industrial Drying, Taylor and Francis, 2007

[6] Bronchart, F, De Paepe, M., Dewulf, J., Schrevens, E., and Demeyer, P., Thermodynamics of greenhouse systems for the northern latitudes: Analysis, evaluation and prospects for primary energy saving, Journal of Environmental Management, pp. 121-133, 2013

[7] van Deventer, H. C. and Heijmans, R. M. H., Drying with superheated steam, Drying Technology, pp. 2033-2045, 2001
[8] Atuonwu, J. C., Energy-efficient low-temperature drying using adsorbents: a Process Systems Engineering approach, 2013,
[9] Mujumdar, A. S., An overview of innovation in industrial drying: current status and R&D needs, Transport in Porous Media, pp. 3-18, 2007
[10] Moran, M. J. and Shapiro, H. N., Fundamentals of engineering thermodynamics, John Wiley&Sons, Chicester,England, 1998
[11] Kessling, W., Laevemann, E., and Kapfhammer, C., Energy storage for desiccant cooling systems component development, Solar Energy, pp. 209-221, 1998
[12] Lowenstein, A. and Gabruk, R. S., The effect of absorber design on the performance of a liquid-desiccant air conditioner, Ashrae Transactions, pp. 712-720, 1992
[13] Lowenstein, A., Slayzak, S., and Kozubal, E., A zero carryover liquid-dessiccant air conditioner for solar applications., ASME International Solar Energy Conference, 2006,
[14] Lowenstein, A., Review of Liquid Desiccant Technology for HVAC Applications, Hvac&R Research, pp. 819-839, 2008
[15] Conde, M. R., Properties of aqueous solutions of lithium and calcium chlorides: formulations for use in air conditioning equipment design, International Journal of Thermal Sciences, pp. 367-382, 2004
[16] Thome, J. R, Wolverine Heat Transfer Engineering data Book III, Laboratory of Heat and Mass transfer (LTCM), Faculty of Engineering Science and Technology, Swiss Federal Institute of Technology Lausanne (EPFL), 2007
[17] VDI, VDI Heat Atlas, Springer, 2010
[18] Bronchart, F, De Paepe, M., and Demeyer, P., Heat-mass transfer system and method. patent Introduction number EP14194300.1, 2014

OPTIMIZATION OF SHELL-AND-TUBE HEAT EXCHANGER USING WIND DRIVEN TECHNIQUE

Emerson Hochsteiner de Vasconcelos Segundo*[1]; Marcos Batistella Lopes[1], Viviana Cocco Mariani[1]
and Leandro dos Santos Coelho[2]
*Author for correspondence
[1]Mechanical Engineering Graduate Program (PPGEM),
[2]Industrial and Systems Engineering Graduate Program (PPGEPS)
Pontifical Catholic University of Parana (PUCPR),
Curitiba, Parana State,
Brazil,
E-mail: e.hochsteiner@gmail.com

ABSTRACT

In the presented work a shell-and-tube heat exchanger is valued using a non-traditional technique, the wind driven optimization algorithm. Shell-and-tube heat exchangers are the most common type of thermal equipment employed in chemical process industries. This widespread use can be justified by its versatility, robustness and reliability. Due to the important role of shell-and-tube heat exchangers, a considerable number of papers has been devoted to the design optimization problem, employing different techniques, such as numerical solution of the stationary point equations of a nonlinear objective function, graphical analysis of the search space, simulated annealing, genetic algorithms, mixed integer nonlinear programming and systematic screening of tube count tables. The wind driven optimization is an optimization metaheuristics algorithm, it is a stochastic nature-inspired global optimization method that is based on atmospheric motion that incorpores the gradient pressure force, friction force, gravitational force and Coriolis force. The traditional design approach of this kind of heat exchanger involves several geometrical parameters and operational constraints. In this paper we focus our study in the proper implementation and evaluation of the nature-inspired technique among other well-known algorithms. The evaluation of the performance of this algorithm is compared with literature, genetic algorithm and particle swarm optimization results. The simulations with WDO proved to achieve better solutions than the other techniques.

Key-words: wind driven optimization, nature-inspired algorithm, metaheuristics, shell-and-tube heat exchangers.

INTRODUCTION

Heat exchangers are used in several industrial processes to recover heat between two fluids there are incorporated to the process. Shell-and-tube heat exchangers (STHE) are the most widely used heat exchangers because of their simple manufacturing and flexibility to different operating conditions [1, 2].

The design of this type of heat exchanger involves several geometrical and operating variables that must achieve a heat duty under certain constrains [3].

There are many previous studies about the optimization of heat exchangers where different techniques were used to optimize the design, adopting different objective functions to accomplish the optimal solution. Chauduri et al. [4] used simulated annealing approach for the optimal design, Selbas et al. [2] and Caputo et al. [5] used genetic algorithm (GA), Ozcelik [6] used mixed integer nonlinear programming, Fesanghary et al. [1] used harmony search, Patel and Rao [7] used particle swarm optimization (PSO), among others.

Among all optimization techniques, the field of global optimization based on metaheuristics has been very active, producing different kinds of stochastic algorithms for optimization in the continuous domain. The search efficiency of metaheuristic algorithms can be attributed to the fact that they are designed to mimic some features in nature with many different sources in biotic and abiotic environment.

The major challenge of the global continuous optimization is that the problems may have many local optima. In the last few decades it can be seen an incredible growth in the field of bio-inspired metaheuristics related to evolutionary algorithms [8-10] and swarm intelligence paradigms [11-13].

The observation of nature processes and how it performs physical, chemical and biological processes provides important leverage in the generation of new bio-inspired methods. The wind driven optimization (WDO) was introduced to the scientific community by Bayraktar et al. [14] and it was shown that the algorithm was easy to implement and effective in solving multidimensional numerical optimization problems. Moreover, there are multiple coefficients that must be chosen to starting an optimization using WDO, including the universal gas constant, the temperature, the gravitational constant, the friction coefficient, and the Coriolis effect.

The main objectives of this paper are, at first, optimize the principal parameters of shell-and-tube heat exchangers from economic point of view considering discount operational costs and, second, demonstrate the effectiveness of wind driven optimization technique comparatively to other techniques, such genetic algorithm and particle swarm optimization, and literature.

NOMENCLATURE

a_1	[€]	Numerical constant
a_2	[€/m²]	Numerical constant
a_3	[-]	Numerical constant
A	[m²]	Cross sectional area normal to flow direction
A_s	[m²]	Heat exchanger surface area
B	[m]	Baffles spacing
C_i	[€]	Capital investiment
C_o	[€/yr]	Annual operating cost
C_{od}	[€]	Total discounted operating cost
C_p	[J/kg K]	Specific heat
C_{tot}	[€]	Total annual cost
d_e	[m]	Equivalent shell diameter
d_i	[m]	Tube inside diameter
d_o	[m]	Tube outside diameter
D_s	[m]	Shell inside diameter
F	[-]	Temperature difference correction factor
f_s	[-]	Shell side friction coefficient
f_t	[-]	Tube side friction coefficient
H	[h/yr]	Annual operating time
h_s	[W/m² K]	Shell side convective coefficient
h_t	[W/m² K]	Tube side convective coefficient
i	[%]	Annual discount rate
k	[W/m K]	Thermal conductivity
L	[m]	Tubes length
LMTD	[K]	Logarithmic mean temperature difference
m_s	[kg/s]	Shell side mass flow rate
m_t	[kg/s]	Tube side mass flow rate
n	[-]	Number of tube passes
ny	[yr]	Equipment life
N_t	[-]	Number of tubes
P	[W]	Pumping power
Pr_s	[-]	Shell side Prandtl number
Pr_t	[-]	Tube side Prandtl number
Q	[W]	Heat duty
Re_s	[-]	Shell side Reynolds number
Re_t	[-]	Tube side Reynolds number
R_{fs}	[m² K/W]	Shell side fouling resistance
R_{ft}	[m² K/W]	Tube side fouling resistance
S_t	[m]	Tube pitch
T_{ci}	[K]	Cold fluid inlet temperature
T_{co}	[K]	Cold fluid outlet temperature
T_{hi}	[K]	Hot fluid inlet temperature
T_{ho}	[K]	Hot fluid outlet temperature
U	[W/m² K]	Overall heat transfer coefficient
v_s	[m/s]	Shell side fluid velocity
v_t	[m/s]	Tube side fluid velocity
ΔP	[Pa]	Pressure drop

Special characters

μ	[Pa s]	Dynamic viscosity
ρ	[kg/m³]	Density
η	[-]	Overall pumping efficiency

Subscripts

c	Cold stream
e	Equivalent
h	Hot stream
i	Inlet
o	Outlet
s	Shell side
t	Tube side
wt	Wall

WIND DRIVEN OPTIMIZATION ALGORITHM

The WDO algorithm takes its inspiration from earth's atmosphere where the wind flow participates of an attempt to balance horizontally the air pressure [15]. The earth's gravitational field acts over the mass of the atmosphere in direction of the crust, where the air pressure is defined by the force exerted by unit of area [16].

The wind blowing comes from the heating due the radiation of the sun over the surface, which occurs irregularly, generating fluctuations of temperature that generates differences of density on the air, where worm air rise and cold air sinks [17]. This movement comes from the pressure gradient that expressed in rectangular coordinates system have the form given by

$$\nabla Pres=\left(\frac{\partial P}{\partial x},\frac{\partial P}{\partial y},\frac{\partial P}{\partial z}\right) \quad (1)$$

The wind blows in the direction of high pressure area to a low pressure area with a velocity proportional to the pressure gradient force, given by

$$F_{PG}=-\nabla Pres\delta V \quad (2)$$

The representation of the atmospheric motion in this model uses the Lagrangian description [18] due to its infinitesimal fluid parcels collection that can be over-ruled by Newton's second law of motion. The Lagrangian description also contributes to reduce the computation overhead during the optimization process because of the simplification of the numerical algorithm considering the air parcel as a cuboid in the rectangular system of coordinates [15]. This abstraction of the WDO considers each air parcel dimensionless, what do not complicate the implementation by separate coordinates for each corner of the cuboid. In addition, each face of the cuboid can receive different pressure values causing it is deformation by several forms.

In the case of wind flow, it is assumed that the atmosphere is a homogeneous fluid and that hydrostatic balance is present. Considering the fact of the rectangular coordinate decryption and that the horizontal movement is stronger than the vertical movement, the wind blows can be treated as horizontal motion only [19]. However, the WDO algorithm can operate under N-dimensional search space considering certain assumptions and simplifications.

The process of the air parcel trajectory calculation starts from the Newton's second law of motion, which states that the total force applied on an air parcel causes its acceleration according to

$$\rho a=\sum F_i \quad (3)$$

where ρ is the density, a is the acceleration and F_i is the external force. The relation of the air parcel pressure and it's density is given by

$$Pres=\rho RT \quad (4)$$

where R is the ideal gas constant and T is the temperature. In this model, the pressure gradient can be considered the fundamental force that initiates the motion of the air parcel, although, that are four different forces that can cause influence on the movement such as pressure gradient force defined

previously, friction force, gravitational force and Coriolis force [14], given respectively by equations given by

$$F_F=-\rho\alpha v \quad (5)$$

$$F_G=\rho\delta Vg \quad (6)$$

$$F_C=-2\Omega xv \quad (7)$$

where g is acceleration of gravity and v is the velocity. These four forces are the major contributors to the motion of air parcel, but there are other forces not considered, for example, advection and turbulent drag force.

Assembling all the forces described in the equation and using the ideal gas law the density can be written in terms of the pressure, where the index c corresponds to the current value of the parameter. In this case, we have the velocity (v) and the position of the air parcel (x) updated by

$$\Delta v=g+\left(-\nabla Pres\frac{RT}{Pres_c}\right)-\alpha u+\left(\frac{-2\Omega xvRT}{Pres_c}\right) \quad (8)$$

Considering that $\Delta v=v_{new}-v_c$, that the acceleration of gravity $g=|g|(0-x_c)$ and $\nabla Pres=|Pres_{opt}-Pres_c|(x_{opt}-x_c)$, we rewrite the equation (8) assuming $Pres_c$ as index i to obtain the equations (9) and (10) where $\Delta t=1$. In this case, we have

$$v_{new}=(1-\alpha)v_c-gx_c+\left(\left|\frac{1}{i}-1\right|(x_{opt}-x_c)RT\right)+\left(\frac{-2\Omega xvRT}{i}\right) \quad (9)$$

$$x_{new}=x_c+(v_{new}\Delta t) \quad (10)$$

The implementation of the WDO starts with the initialization of the parameters population size, maximum number of iterations, coefficients, boundaries and pressure function definition that compounds the objective function. Than allocate random positions and velocities for the air parcels for the evaluation of the pressure for each air parcel and the update of velocity and position and it is checking under the velocity limits and boundaries conditions until the maximum number of iterations as stopping criterion.

MATHEMATICAL MODEL

The typical arrangement of the shell-and-tube heat exchanger is shown in **Figure 1**.

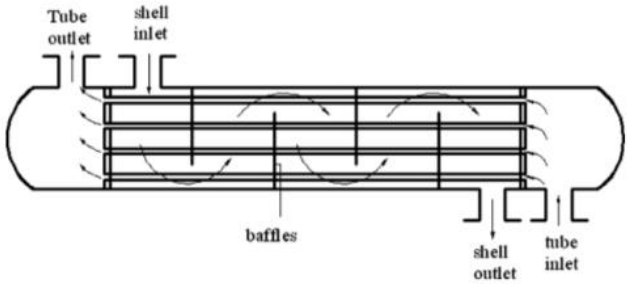

Figure 1 Typical arrangement of STHE [21].

The mathematical description of the heat exchanger was taken from Patel and Rao [7] and some adaptations were made for better comprehension by these authors.

According to the flow regime the tube side heat transfer coefficient for $Re_t > 10000$ is obtained from

$$h_t=0.027\frac{k_t}{d_o}Re_t^{0.8}Pr_t^{0.33}\left(\frac{\mu_t}{\mu_{wt}}\right)^{0.14} \quad (11)$$

where $\mu_{wt} = 0.000175$ [Pa s] and Re_t is given as

$$Re_t=\frac{\rho_t v_t d_i}{\mu_t} \quad (12)$$

where $d_i = 0.8d_o$.

Pr_t is the Prandtl number given as

$$Pr_t=\frac{\mu_t Cp_t}{k_t} \quad (13)$$

Kern's formulation [3] for segmental baffle shell-and-tube heat exchanger is used for shell side heat transfer coefficient, obtained from

$$h_s=0.36\frac{k_t}{d_e}Re_s^{0.55}Pr_s^{0.33}\left(\frac{\mu_s}{\mu_{wts}}\right)^{0.14} \quad (14)$$

where $\mu_{wts} = 0.00039$ [Pa s] and d_e is the shell hydraulic diameter for triangular pitch given as

$$d_e=\frac{4(0.43s_t^2-(0.125\pi d_o^2))}{0.5\pi d_o} \quad (15)$$

where $S_t = 1.25d_o$.

The cross section area normal to flow direction is obtained from

$$A_s=0.2D_sB \quad (16)$$

Flow velocity for the shell side is given as

$$v_s=\frac{m_s}{\rho_s A_s} \quad (17)$$

Reynolds number for shell side is obtained from

$$Re_s=\frac{m_s d_e}{A_s\mu_s} \quad (18)$$

Prandtl number for shell side is obtained from

$$Pr_s=\frac{\mu_s Cp_s}{k_s} \quad (19)$$

The overall heat transfer coefficient is given as

$$U=\frac{1}{(h_s^{-1}+R_{fs}+1.25(R_{ft}+h_t^{-1}))} \quad (20)$$

The logarithmic mean temperature difference is

$$LMTD=\frac{(T_{hi}-T_{co})-(T_{ho}-T_{ci})}{\ln\left((T_{hi}-T_{co})(T_{ho}-T_{ci})^{-1}\right)} \quad (21)$$

The correction factor for the configuration is given as

$$F=\frac{\sqrt{1+R^2}\ln\left((1-P)(1-PR)^{-1}\right)}{(R-1)\ln\left(\left(3-PR-\sqrt{R^2+1}\right)\left(3-PR+\sqrt{R^2+1}\right)^{-1}\right)} \quad (22)$$

where R is the correction coefficient and P is the efficiency and both are obtained from

$$R=\frac{T_{hi}-T_{ho}}{T_{co}-T_{ci}} \quad (23)$$

$$P=\frac{T_{co}-T_{ci}}{T_{hi}-T_{ci}} \quad (24)$$

The exchanger surface area is given as

$$A=\frac{Q}{UFLMTD} \quad (25)$$

Based on exchanger surface area the tube length is determined by

$$L=\frac{A}{\pi d_o N_t} \quad (26)$$

The tube side pressure drop is obtained from

$$\Delta P_t=\frac{\rho_t v_t^2}{2}\left(\frac{L}{d_i}ft+2.5\right)n \quad (27)$$

where n = 2 and $ft = (1.82\log(Re_t)-1.64)^{-2}$.

The shell side pressure drop is obtained from

$$\Delta P_s=1.44Re_s^{-0.15}\left(\frac{\rho_s v_s^2}{2}\right)\left(\frac{L}{B}\right)\left(\frac{D_s}{d_e}\right) \quad (28)$$

for $Re_s<40000$.

Considering pumping efficiency η = 0.25, the pumping power is given as

$$P=\frac{1}{\eta}\left(\frac{m_s}{\rho_s}\Delta P_s+\frac{m_t}{\rho_t}\Delta P_t\right) \quad (29)$$

Based on all above calculations the objective function [5], is

$$C_{tot}=C_i+C_{od} \quad (30)$$

where C_i and C_{od} are given as

$$C_i=8000+259.2A^{0.93} \quad (31)$$

$$C_{od}=\sum_{x=1}^{ny}\frac{C_o}{\left(1+\frac{i}{100}\right)^x} \quad (32)$$

where $C_o = PC_eH$.

From the above equations it can be observed that the variables that must be search by iteration in the objective function are D_s, B, d_o and N_t.

Case Study

The case study chosen for the application of the WDO technique was a problem explored in the literature and by Caputo et al. [5] and Patel and Rao [7] that consists in a shell-and-tube heat exchanger with two tube passages and one shell passage of methanol-blackish water with 4.34 MW of duty heat. **Table 1** presents the values for process inputs and physical properties of the components.

Table 1 The process inputs and physical properties for the case study [5, 7].

	Shell side (methanol)	Tube side (sea water)
Mass flow (kg/s)	27.80	68.90
T_{input} (K)	368	298
T_{output} (K)	313	313
ρ (kg/m³)	750	995
C_p (J/kg K)	2840	4200
μ (Pa s)	0.00034	0.0008
K (W/m K)	0.19	0.59
$R_{fouling}$ (m² K/W)	0.00033	0.0002

In the WDO approach some boundary were imposed for D_s, between 0.1 m and 1.5 m, for d_o, between 0.015 m and 0.051 m, for B, between 0.05 m and 0.5 m and for N_t, between 800 and 2000. All the values of discounted operating costs are computed with ny equal to 10 yr, annual discount rate i equal to 10% and energy cost C_e equal to 0.00012 €/W h with an annual amount of work hours of 7000 h/yr [7].

The parameters for the WDO were suggested by [9] were - $2\Omega RT$ equal to 0.4, RT equal to 3, g equal to 0.2, α equal to 0.4 and maximum velocity equal to 0.3 and 1, this last value of maximum velocity were chosen because of the comparison with de PSO technique [7]. Initial population equal to 50, number of iterations equal to 100 and 50 runs were applied [7].

RESULTS

The results of the simulations are presented in **Table 2** were a comparison between the literature [3, 20], the results by Caputo et al. [5] with GA and the results by Patel and Rao [7] with PSO are made.

It can be observed that very similar values were obtained from the techniques using both maximum velocities equal to 0.3 and equal to 1.0.

Although the results obtained becomes important to note that in the work presented by Mariani et al. [22] similar comparison are made using quantum-behaved particle swarm approaches and better results were achieved with results for the cost optimization reaching values under 45,000 € for total annual cost (C_{tot}). It is important to notice that in this work differences in the values of the parameters were found in comparison with the traditional techniques, such as GA and PSO.

Table 2 Optimal heat exchanger geometry using different optimization methods.

	Literature [3, 20]	GA [5]	PSO [7]	$WDO_{0.3}$	$WDO_{1.0}$
L (m)	4.83	3.379	3.115	1.247	1.216
d_o (m)	0.02	0.016	0.015	0.026	0.026
B (m)	0.356	0.5	0.424	0.5	0.5
D_s (m)	0.894	0.83	0.81	0.7	0.7
S_t (m)	0.025	0.02	0.0187	0.0323	0.0328
N_t	918	1567	1658	1979	2000
v_t (m/s)	0.75	0.69	0.67	0.70	0.70
Re_t	14925	10936	10503	18008	18316
Pr_t	5.7	5.7	5.7	5.69	5.69
h_t (W/m² K)	3812	3762	3721	3453	3442
f_t	0.028	0.031	0.0311	0.0268	0.0267
ΔP_t (Pa)	6251	4298	4171	1219	1219
d_e (m)	0.014	0.011	0.0107	0.018	0.018
v_s (m/s)	0.58	0.44	0.53	0.53	0.53
Re_s	18381	11075	12678	21496	21960
Pr_s	5.1	5.1	5.1	5.08	5.08
h_s (W/m² K)	1573	1740	1950.8	4699.6	4675.3
ΔP_s (Pa)	35789	13267	20551	3217	3115
U (W/m² K)	615	660	713.9	866	864
A (m²)	278.6	262.8	243.2	200.4	200.8
C_i (€)	51507	49259	46453	43847.1	43914.5
C_{od} (€)	12973	5818	6778.2	5006.7	4913.5
C_{tot} (€)	64480	55077	53231.1	48853.8	48828

The best results were obtained from the simulations using WDO_1, it can be observed that the pressure drops were also lower than the other techniques. It was observed that in both cases the convergence occurred under 10 iterations. The difference of the values obtained for total annual cost is presented in **Table 3**.

Table 3 Percentual difference of total annual cost between optimization methods and literature.

	Literature [3, 20]	GA [5]	PSO [7]
$WDO_{0.3}$	24.23%	11.30%	8.22%
WDO_1	24.27%	11.35%	8.27%

Both WDO applications obtained better results among the methods in comparison and literature, indicating that the technique has robustness.

CONCLUSION

Heat exchangers are an important component of any thermal system and their designs should be adapted for the applications required for purpose use, otherwise additional costs may occur. The present study has demonstrated the application of WDO technique for the optimal design of shell-and-tube heat exchanger from economic point of view, consisting in simple concept and easy implementation. The WDO technique converged to optimum value of the objective function with few generations and with total annual cost lower than other techniques, GA and PSO, with values between 8% and 25% less total annual cost.

Future studies could be encouraged for an improvement of the WDO algorithm applying different values of the parameters or promoting ways of determining these values also iteratively. The application of the WDO technique considering other components in shell-and-tube heat exchangers could be explored.

REFERENCES

[1] Fesanghary M., Damangir E., Soleimani L., Design optimization of Shell-and-tube heat exchangers using global sensitivity analysis and harmony search algorithm, *Applied Thermal Engineering*, Vol. 29, 2009, pp 1026-1031.

[2] Selbas R., Kizilkan O., Reppich M., A new design approach for shell-and-tube heat exchangers using genetic algorithms from economic point of view, *Chemical Engineering and Processing*, Vol. 45, 2006, pp 268-275.

[3] Kern D.Q., *Process Heat Transfer*, McGraw-Hill, New York, 1950.

[4] Chauduri P.D., Diwekar U., Logsdon J., An automated approach for the optimal design of heat exchangers, *Industrial & Engineering Chemistry Research*, Vol. 36, 1997, pp 3685-3693.

[5] Caputo A.C., Pelagagge P.M., Salini P., Heat exchanger design based on economic optimization, *Applied Thermal Engineering*, Vol. 27, 2007, pp 1151-1159.

[6] Ozcelik Y., Exergetic optimization of shell-and-tube heat exchanger using a genetic based algorithm, *Applied Thermal Engineering*, Vol. 27, 2007, pp 1849-1856.

[7] Patel V.K., Rao R.V., Design optimization of shell-and-tube heat exchanger using particle swarm optimization technique, *Applied Thermal Engineering*, Vol. 30, 2010, pp 1417-1425.

[8] Back T., Fogel D., Michalewicz Z., *Handbook of Evolutionary Computation*, Oxford University Press, New York, 1997.

[9] Das S., Suganthan P.N., Differential evolution: a survey of the state-of-the-art, *IEEE Transactions on Evolutionary Computation*, Vol. 15, no. 1, 2011, pp. 4-31.

[10] Das S., Maity S., Qu B.Y., Suganthan P.N., Real-parameter evolutionary multimodal optimization — A survey of the state-of-the-art, *Swarm and Evolutionary Computation*, Vol. 1, no. 2, 2011, pp. 71-88.

[11] Kennedy J., Eberhart R.C., Shi Y., *Swarm Intelligence*, Morgan Kaufman, San Francisco, 2001.

[12] Engelbrecht A.P., *Fundamentals of Computational Swarm Intelligence*, John Wiley & Sons, Hoboken, 2006.

[13] Yang X.S., *Engineering Optimization: An Introduction with Metaheuristic Applications*, John Wiley & Sons, United Kingdom, 2010.

[14] Bayraktar Z., Komurcu M., Wener D.H., Wind driven optimization (WDO): A novel nature-inspired optimization algorithm and its application to electromagnetic, *Proceedings of the IEEE International Symposium on Antennas and Propagation and CNC/USNC/URSI Radio Science Meeting*, Toronto, Canada,11-17 July, 2010.

[15] Bayraktar Z., Komurcu M., Bossard J.A., The wind driven optimization technique and its application in eletromagnetics, *IEEE Transactions on Antennas and Propagation*, Vol. 61, no. 5, 2013, pp. 2745-2757.

[16] Riehl H., *Introduction to the Atmosphere*, Mc-Graw Hill, New York, 1978.

[17] Ahrens C.D., *Meteorology Today: An Introduction to Weather, Climate, and the Environment*, 7th ed., Thomson-Brook/Cole, Belmont, 2003.

[18] Stull R.B., *Meteorology for Scientists and Engineers*, 2nd ed., Brooks/Cole, Belmont, 1999.

[19] Thompson R.D., *Atmospheric Processes and System*, Routledge, New York, 1998.

[20] Sinnot R.K., Coulson J.M., Richardson J.F., *Chemical Engineering Design*, Vol. 6, Butterworth-Heinemann, Boston, 1996.
[21] Guo J., Cheng L., Xu M., Optimization design of shell-and-tube heat exchanger by entropy generation minimization and genetic algorithm, *Applied Thermal Engineering*, Vol. 29, 2009, pp 2954-2960.
[22] Mariani V.C., Duck A.R.K., Guerra F.A., Coelho L.S., Rao R.V., A chaotic quantum-behaved particle swarm approach applied to optimization of heat exchangers, *Applied Thermal Engineering*, Vol. 42, 2012, pp 119-128.